Three-dimensional small-scale instabilities of plane internal gravity waves

Sasan John Ghaemsaidi[1],† and Manikandan Mathur[2],†

[1]Huntsville, AL 35806, USA

[2]Department of Aerospace Engineering, Indian Institute of Technology Madras, Chennai - 600036, India

We study the evolution of three-dimensional (3-D), small-scale, small-amplitude perturbations on a plane internal gravity wave using the local stability approach. The plane internal wave is characterised by its non-dimensional amplitude, A, and the angle the group velocity vector makes with gravity, Φ. For a given (A, Φ), the local stability equations are solved on the periodic fluid particle trajectories to obtain growth rates for all two-dimensional (2-D) and 3-D perturbation wave vectors. For small A, the local stability approach recovers previous results of 2-D parametric subharmonic instability (PSI) while offering new insights into 3-D PSI. Higher-order triadic resonances, and associated deviations from them, are also observed at small A. Moreover, for small A, purely transverse instabilities resulting from parametric resonance are shown to occur at select values of Φ. The possibility of a non-resonant instability mechanism for transverse perturbations at finite A allows us to derive a heuristic, modified gravitational instability criterion. We then study the extension of small A to finite A internal wave instabilities, where we recover and build upon existing knowledge of small-scale, small-amplitude internal wave instabilities. Four distinct regions of the (A, Φ)-plane based on the dominant instability modes are identified: 2-D PSI, 3-D oblique, quasi-2-D shear-aligned, and 3-D transverse. Our study demonstrates the local stability approach as a physically insightful and computationally efficient tool, with potentially broad utility for studies that are based on other theoretical approaches and numerical simulations of small-scale instabilities of internal waves in various settings.

Key words: geophysical and geological flows, instability, internal waves

---

1. Introduction

Spatial and temporal growth of small-amplitude perturbations represent important pathways towards dissipation, and subsequently mixing, for internal gravity waves in the atmosphere, ocean and planetary systems. Moreover, wave instabilities are potentially relevant for understanding the internal wave spectra observed in the ocean (Garrett & Munk 1975). A myriad of linear instabilities have previously been identified in internal waves of various spatial profiles, summaries of which can be

† Email addresses for correspondence: ghaemsaidi@alum.mit.edu, manims@ae.iitm.ac.in

found in Lombard & Riley ([1996]), Sonmor & Klaassen ([1997]), Staquet & Sommeria ([2002]) and Dauxois *et al.* ([2018]).

Heuristic arguments and approximations based on static vertical profiles have been useful in identifying certain instabilities in large-amplitude internal waves (Fritts & Yuan [1989]; Thorpe [1994]), although they are also known to ignore important dynamical effects (Hines [1971]). By contrast, Floquet theory fully incorporates, and takes advantage of, the spatial and temporal periodicity of plane internal waves while placing no restriction on the amplitude (Mied [1976]; Drazin [1977]; Klostermeyer [1982]). Additionally, Floquet theory makes no assumptions on the spatial scale of the perturbations, although it relies on the assumption of small-amplitude perturbations, and requires the truncation of an infinite sum in its solution, with the required number of terms being greater for larger internal wave amplitudes (Sonmor & Klaassen [1997]). For certain large-amplitude internal waves, the required number of terms in the Floquet sum can be several hundred, thus significantly increasing the computational requirement to solve the resulting eigenvalue problem for a given perturbation wave vector. Furthermore, the solution form in Floquet theory, as assumed in Sonmor & Klaassen ([1997]), is not applicable if the temporal or spatial periodicity of the internal wave field does not hold, e.g. a plane internal wave with steady background shear or an internal wave beam.

Using Floquet theory alongside an energy budget analysis, Lombard & Riley ([1996]) calculated and characterised two-dimensional (2-D) and three-dimensional (3-D) instabilities of finite amplitude internal gravity waves. Lombard & Riley ([1996]) concluded that small-amplitude plane internal waves can succumb to 2-D instabilities related to second-order wave–wave interactions, and that large-amplitude plane internal waves are also prone to 3-D instabilities that may be related to higher-order resonant interactions. Using a similar approach, Sonmor & Klaassen ([1997]) showed that the dominant linear instabilities in large-amplitude plane internal waves can be traced back to resonant instabilities at small amplitude. These resonant wave–wave interactions, which underlie the instabilities of large-amplitude internal waves observed by Lombard & Riley ([1996]) and Sonmor & Klaassen ([1997]), comprise the formation of a resonant wave triad between the primary internal wave and two perturbation waves. The particular class of triads corresponding to small-scale perturbations propagating at half the temporal frequency of the primary wave is known as parametric subharmonic instability (PSI) (McEwan & Robinson [1975]), and has been the subject of several experimental (Bourget *et al.* [2013]) and numerical (Koudella & Staquet [2006]) studies. The potential for PSI to serve as a mechanism that can transfer energy from large to small scales has made them the subject of studies focusing on oceanic phenomena (McComas & Bretherton [1977]; MacKinnon & Winters [2005]). Apart from PSI, higher-order resonant interactions that lead to the growth of shear-aligned perturbations at a frequency that is half of an integer multiple of the primary wave frequency have also been studied (Sonmor & Klaassen [1996]). As we will show, the local stability approach that we employ in this paper recovers some well-established features of PSI and higher-order resonance occurring for small-amplitude internal waves.

The local stability equations (Lifschitz & Hameiri [1991]), which are a set of ordinary differential equations governing the evolution of perturbation amplitude and wave vector on fluid particle trajectories in the base flow, are restricted to perturbations whose spatial scales are small relative to the base flow length scale. Being much simpler to solve than the corresponding linear stability equations that govern perturbations of arbitrary spatial scales, the local stability equations have

proven to be very useful in identifying and analysing short-wavelength instabilities in steady but strongly non-parallel flows such as a vortex. Local stability studies have focused on the centrifugal (Sipp & Jacquin 2000; Nagarathinam, Sameen & Mathur 2015), elliptic (Bayly 1986) and hyperbolic (Leblanc 1997) instabilities in a number of idealized vortex models that incorporate the effects of background rotation (Godeferd, Cambon & Leblanc 2001), stratification (Miyazaki & Fukumoto 1992) or a combination of these factors (Miyazaki 1993). The local stability approach has also been applied to unsteady vortex models (Bayly, Holm & Lifschitz 1996). Moreover, the instabilities of vortical or tidal motions of stratified fluids have been shown, using local stability theory, to resonantly excite internal gravity waves (Miyazaki & Fukumoto 1992; Le Reun, Favier & Le Bars 2018). The correspondence between the local and global (normal mode) stability approaches, however, remains an intriguing question, although some studies (Sipp & Jacquin 2000; Mathur *et al.* 2014) have reported on this aspect for the centrifugal instability; local stability studies of numerically simulated 2-D vortex flows have also performed some comparisons with the growth rates obtained from global stability analyses (Gallaire, Marquillie & Ehrenstein 2007; Aravind, Mathur & Dubos 2017). Recent local stability studies of geophysical flows have helped identify small-scale instabilities of Gerstner's waves (Leblanc 2004), equatorially trapped waves (Constantin & Germain 2013) and edge waves on a sloping beach (Ionescu-Kruse 2014, 2015).

In this paper, we elucidate the various small-scale 2-D and 3-D linear instabilities of a plane internal gravity wave using the local stability approach. In doing so, we demonstrate the local stability approach to be a physically insightful and computationally efficient tool to study internal waves in various settings. It is worth highlighting that it is *a priori* unknown which instabilities present in a global stability approach, like the Floquet theory of Mied (1976) and Sonmor & Klaassen (1997), may be captured in our local stability analysis. As we will show, the local stability approach recovers established results of small-scale internal wave instabilities, and sheds light on previously unexplored 3-D instabilities.

The paper is organized as follows. Section 2 presents a description of the base flow, and the local stability equations that govern the evolution of small-scale perturbations of plane internal waves. In § 3, we present our calculations and results spanning a large range of non-dimensional wave amplitudes and orientation angles, and offer comparisons with previous literature. A geophysical application of the local stability approach is presented in § 4. Finally, a summary of our results followed by conclusions and suggestions for future work are presented in § 5.

2. Theory

We consider an unbounded, non-rotating, uniformly stratified fluid of constant buoyancy frequency N. The total velocity $\boldsymbol{U}$, pressure P and buoyancy B fields are a superposition of small-amplitude, short-wavelength perturbations onto an internal wave base flow:

$$\boldsymbol{U} = \bar{\boldsymbol{u}} + \boldsymbol{u}', \tag{2.1}$$

$$P = -\bar{\bar{\rho}} g z + \bar{p} + p', \tag{2.2}$$

$$B = \bar{\bar{b}} + \bar{b} + b', \tag{2.3}$$

where $\bar{\bar{\rho}}(z) = \rho_0 - (\rho_0/g)N^2 z$ is the stable background linear density stratification; $\bar{\bar{b}} = (\bar{\bar{\rho}}/\rho_0)g$ is the background buoyancy field; ρ_0 is a reference density; $\bar{\boldsymbol{u}}$, $\bar{p}$ and $\bar{b}$ are the

velocity, pressure and buoyancy fields of the internal wave, respectively, (u', p', and b' are the corresponding perturbation fields); and $g = -g\hat{e}_z$ is gravity. The momentum, incompressibility and mass conservation equations – under the inviscid, non-diffusive, Boussinesq approximations – are, respectively,

$$U_t + U \cdot \nabla U = -\nabla(P/\rho_0) - B\hat{e}_z, \qquad (2.4)$$

$$B_t + U \cdot \nabla B = 0, \qquad (2.5)$$

$$\nabla \cdot U = 0. \qquad (2.6)$$

The base flow is described by a 2-D plane internal gravity wave:

$$\bar{\psi} = \Psi \cos(k \cdot x - \omega t), \quad \bar{p} = -\frac{\rho_0 \omega}{k} \bar{\psi}_z, \quad \bar{b} = -\frac{kN^2}{\omega} \bar{\psi}, \qquad (2.7a\text{-}c)$$

subject to the dispersion relation:

$$\frac{\omega}{N} = \pm \frac{k}{|k|} = \pm \cos \Phi, \qquad (2.8)$$

where $\bar{\psi}$ is the streamfunction of the velocity field $\bar{u} = (-\bar{\psi}_z, 0, \bar{\psi}_x)$, Ψ is the streamfunction amplitude, $x = (x, y, z)$ is the spatial coordinate, $k = (k, 0, m)$ is the wave vector, t is time, ω is the wave frequency and Φ is the inclination angle of the wave vector k to the horizontal x-axis (or alternatively, the inclination of the constant phase lines to the vertical z-axis), as shown in figure 1. We note that (2.7a–c) are solutions to the linearised and fully nonlinear version of (2.4)–(2.6), and that equations (2.7b,c) follow from the linearised forms of (2.4) and (2.5), respectively (see Tabaei & Akylas 2003, § 2).

Using (2.8) to compute the group velocity vector $c_g = (\partial_k \omega, 0, \partial_m \omega)$, one finds that as Φ, and thus k, approach the x-axis, c_g approaches the z-axis by virtue of k and c_g being orthogonal (see Kundu, Cohen & Dowling 2012, § 7.8). As a result, the internal wave energy propagates at a steep (shallow) angle for small (large) Φ. Figure 1 illustrates the internal wave base flow and relevant system parameters.

Choosing N^{-1} and $|k|^{-1}$ as representative time and length scales, respectively, we write the following dimensionless parameters to characterise the base flow:

$$A = \frac{|k|^2}{N} \Psi, \quad \Phi = \tan^{-1}\left(\frac{m}{k}\right), \qquad (2.9a,b)$$

where A is the dimensionless net-velocity amplitude of the base flow and Φ is a measure of the base flow orientation. We introduce a metric of isopycnal steepness defined as

$$s = \frac{\max(\bar{u})}{c_x} = A \sin \Phi, \qquad (2.10)$$

where $\max(\bar{u})$ is the maximum horizontal velocity of the base flow and $c_x = \omega/k$ is the horizontal phase velocity. The condition $s > 1$ is sufficient for the existence of at least one time instance during the internal wave period when overturned isopycnals occur, i.e. $\partial_z(\bar{\rho} + \rho) > 0$. The characteristics of such locally overturned regions are known to be related to internal wave breaking (Thorpe 1994).
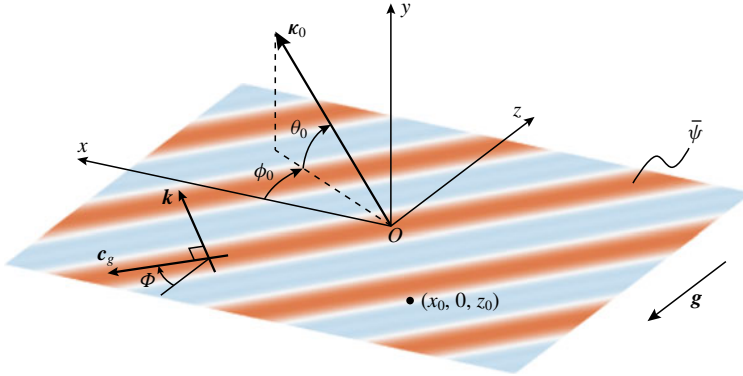
FIGURE 1. (Colour online) An illustration of the base flow $\bar{\psi}$: a plane internal gravity wave in the (x, z)-plane. The initial wave vector $\boldsymbol{\kappa}_0$ of the perturbation that is superposed onto the base flow makes an angle θ_0 with its projection on the (x, z)-plane, and its projection on the (x, z)-plane makes an angle ϕ_0 with the x-axis. The angle Φ is the inclination angle of the base flow wave vector (group velocity vector) relative to the x-axis (z-axis).

Following Lifschitz & Hameiri (1991), we write the short-wavelength perturbations, which we superimpose onto the base flow, in the Wentzel–Kramers–Brillouin–Jeffreys (WKBJ) form:

$$(\boldsymbol{u}', p', b') = \exp(\mathrm{i}\Theta/\varepsilon)[(\boldsymbol{a}, p, b) + \varepsilon(\boldsymbol{a}_\varepsilon, p_\varepsilon, b_\varepsilon) + \cdots], \tag{2.11}$$

where $\boldsymbol{a}(\boldsymbol{x}, t)$, $p(\boldsymbol{x}, t)$ and $b(\boldsymbol{x}, t)$ are, respectively, the complex leading order velocity, pressure and buoyancy perturbation amplitudes, $\Theta(\boldsymbol{x}, t)$ is a real-valued phase function, $0 < \varepsilon \ll 1$ is the parameter reflecting the length scale ratio of the perturbation to the base flow and $\boldsymbol{\kappa} = \nabla\Theta/\varepsilon$ is the perturbation wave vector. Substituting (2.11) into (2.4)–(2.6) and retaining $O(\varepsilon^{-1})$ and $O(\varepsilon^0)$ terms yields the following equations governing the evolution of the perturbation wave vector $\boldsymbol{\kappa}$ and the leading order perturbation amplitudes $(\boldsymbol{a}, b)$ (Miyazaki & Fukumoto 1992):

$$\frac{\mathrm{d}\boldsymbol{\kappa}}{\mathrm{d}t} = -(\nabla\bar{\boldsymbol{u}})^\top \cdot \boldsymbol{\kappa}, \tag{2.12}$$

$$\frac{\mathrm{d}\boldsymbol{a}}{\mathrm{d}t} = -\nabla\bar{\boldsymbol{u}} \cdot \boldsymbol{a} - b\hat{\boldsymbol{e}}_z + \frac{\boldsymbol{\kappa}}{|\boldsymbol{\kappa}|^2}[2(\nabla\bar{\boldsymbol{u}} \cdot \boldsymbol{a}) \cdot \boldsymbol{\kappa} + b\hat{\boldsymbol{e}}_z \cdot \boldsymbol{\kappa}], \tag{2.13}$$

$$\frac{\mathrm{d}b}{\mathrm{d}t} = -\boldsymbol{a} \cdot \nabla(\bar{\bar{b}} + \bar{b}), \tag{2.14}$$

where $\mathrm{d}/\mathrm{d}t = \partial_t + \bar{\boldsymbol{u}} \cdot \nabla$ is the material time derivative with respect to the base flow $\bar{\boldsymbol{u}}$. The local stability equations, (2.12)–(2.14), are, therefore, ordinary differential equations to be solved on fluid particle trajectories in the base flow. We will hereafter be working in a dimensionless framework, using $|\boldsymbol{k}|^{-1}$, N^{-1} and $N^2|\boldsymbol{k}|^{-1}$ as the length, time and buoyancy scales, respectively.

Fluid particle trajectories $\bar{\boldsymbol{x}}(t) = (\bar{x}, 0, \bar{z})$ in the base flow are given by

$$\bar{\boldsymbol{x}} = \boldsymbol{x}_0 + A(\tan\Phi, 0, -1)[\cos(\vartheta_0 - \cos\Phi t) - \cos\vartheta_0], \tag{2.15}$$

where $\boldsymbol{x}_0 = (x_0, 0, z_0)$ is the initial particle position at $t = 0$ and $\vartheta_0 = \cos \Phi x_0 + \sin \Phi z_0$. With no loss of generality, we assume $(x_0, z_0) = (0, 0)$, as all trajectories on the (x, z)-plane are equivalent for a plane wave. All fluid particle trajectories, irrespective of initial location, are periodic in time, i.e. $\bar{\boldsymbol{x}}(t = 2\pi / \cos \Phi) = \bar{\boldsymbol{x}}(t = 0)$.

Since the local stability equations (2.12)–(2.14) are linear in $\boldsymbol{\kappa}$, it suffices to consider only initial perturbation wave vectors of unit magnitude:

$$\boldsymbol{\kappa}_0(\phi_0, \theta_0) = \cos \theta_0 \cos \phi_0 \hat{\boldsymbol{e}}_x + \sin \theta_0 \hat{\boldsymbol{e}}_y + \cos \theta_0 \sin \phi_0 \hat{\boldsymbol{e}}_z, \qquad (2.16)$$

where θ_0 is the angle made by $\boldsymbol{\kappa}_0$ with its projection on the (x, z)-plane, and ϕ_0 is the angle that the projection of $\boldsymbol{\kappa}_0$ on the (x, z)-plane makes with the x axis (see figure 1); $\theta_0 = 0°$ corresponds to 2-D perturbations and any $\theta_0 > 0°$ corresponds to 3-D perturbations. The limit $\theta_0 = 90°$ represents a wave vector aligned entirely along the y axis, i.e. purely transverse perturbations, where the value of ϕ_0 is irrelevant. Equation (2.12), subject to the initial condition (2.16), is solved for the perturbation wave vector to give

$$\boldsymbol{\kappa} = \boldsymbol{\kappa}_0 + A(\sin \Phi \kappa_{0,x} - \cos \Phi \kappa_{0,z})(1, 0, \tan \Phi)[\sin(\vartheta_0 - \cos \Phi t) - \sin \vartheta_0], \quad (2.17)$$

where $\kappa_{0,x}$ and $\kappa_{0,z}$ are the x and z components of the initial perturbation wave vector $\boldsymbol{\kappa}_0$, respectively. For all (A, Φ), every $\boldsymbol{\kappa}$ specified by an initial condition (ϕ_0, θ_0) in the range $[0°, 360°] \times [-90°, 90°]$ is periodic over one internal wave time period. Thus, the growth rate associated with every $\boldsymbol{\kappa}_0$ is computed following the approach of Mathur *et al.* (2014).

A fourth-order Runge–Kutta scheme is used to numerically solve (2.13) and (2.14), for $\boldsymbol{\kappa}$ spanning various (ϕ_0, θ_0), along $\bar{\boldsymbol{x}}$ (with a temporal resolution such that one internal wave period is represented using 500 points). We use four different initial condition vectors of the form $\boldsymbol{c}_0 = [a_{x,0} \ a_{y,0} \ a_{z,0} \ b_0]$ such that the initial condition matrix, $[\boldsymbol{c}_{0,1}; \ \boldsymbol{c}_{0,2}; \ \boldsymbol{c}_{0,3}; \ \boldsymbol{c}_{0,4}]$, is equal to the identity matrix. Thus, for each $\boldsymbol{c}_0$, we numerically obtain amplitude vectors at $t = 2\pi / \cos \Phi$ as $\boldsymbol{c}_{f,1} = [a_{x,1} \ a_{y,1} \ a_{z,1} \ b_1]$, $\boldsymbol{c}_{f,2} = [a_{x,2} \ a_{y,2} \ a_{z,2} \ b_2]$, $\boldsymbol{c}_{f,3} = [a_{x,3} \ a_{y,3} \ a_{z,3} \ b_3]$, and $\boldsymbol{c}_{f,4} = [a_{x,4} \ a_{y,4} \ a_{z,4} \ b_4]$. The instability growth rates are then calculated as (Chicone 2000)

$$\sigma = \frac{\max(\text{Re}(\log(\text{eigenvalues of } \boldsymbol{M})))}{2\pi / \cos \Phi}, \qquad (2.18)$$

where $\boldsymbol{M} = [\boldsymbol{c}_{f,1}; \ \boldsymbol{c}_{f,2}; \ \boldsymbol{c}_{f,3}; \ \boldsymbol{c}_{f,4}]$. The growth rate σ is periodic over $\phi_0 \in [0°, 180°]$ and symmetric about $\theta_0 = 0°$; our subsequent analysis of σ is, therefore, presented over $\phi_0 \in [0°, 180°]$ and $\theta_0 \in [0°, 90°]$. We moreover note that σ is dimensionless, with a growth rate scale of N.

3. Results

3.1. *Instability growth rates*

In figure 2, we present the growth rate σ (2.18) over the (ϕ_0, θ_0)-plane for nine different pairs of base flow parameters (A, Φ). As noted in §2, the growth rates are periodic in ϕ_0 over $[0°, 180°]$ and symmetric about $\theta_0 = 0°$. In figure 2, the internal wave base flow progresses from steep $(\Phi = 15°)$ in the leftmost column to shallow $(\Phi = 75°)$ in the rightmost column, and from small-amplitude $(A = 0.1)$ in the top row to large-amplitude $(A = 10)$ in the bottom row.
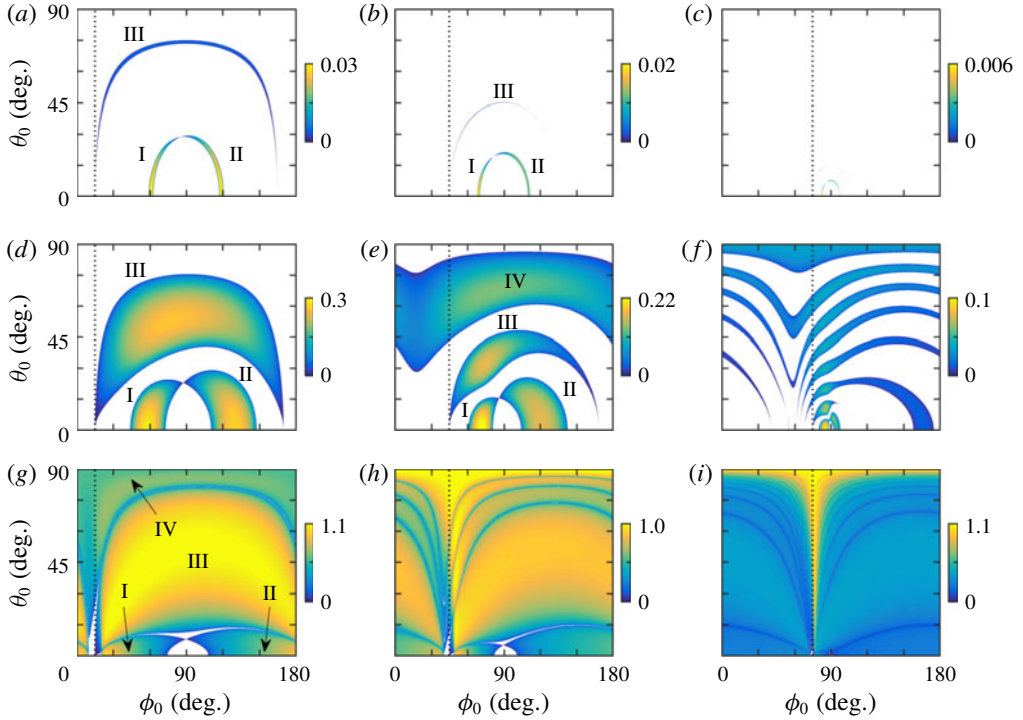
FIGURE 2. (Colour online) Growth rate, σ, presented as a function of ϕ_0 and θ_0 for $A = 0.1$, 1, 10 (top, middle and bottom rows, respectively), and $\Phi = 15°$, $45°$, $75°$ (left, middle and right columns, respectively). Stable regions of the (ϕ_0, θ_0)-plane where $\sigma < 10^{-10}$ have been coloured white. The dotted vertical lines in each panel denote $\phi_0 = \Phi$.

For $(A, \Phi) = (0.1, 15°)$, i.e. small-amplitude, steep internal waves (figure 2a), we observe, in the limit of 2-D perturbations ($\theta_0 = 0°$), two thin instability peaks centred at $\phi_0 = 61°$ and $\phi_0 = 119°$. These instability peaks extend towards regions of 3-D perturbations ($\theta_0 > 0°$) to form two instability ridges on the (ϕ_0, θ_0)-plane; the two instability ridges, labelled I and II in figure 2(a), seem to have similar maximum growth rates, both of which occur on the $\theta_0 = 0°$ axis. Significantly, the growth rates on the $\theta_0 > 0°$ portions of the ridges are comparable to those on the $\theta_0 = 0°$ axis, suggesting that a continuous range of perturbation wave vectors on these ridges are of similar growth rates. It is also noteworthy that the variation of σ with θ_0 on ridges I and II is different, with ridge II retaining larger values of σ up to larger θ_0. As θ_0 approaches a threshold value of $29°$, the two instability ridges approach each other; above the threshold θ_0, ridges I and II vanish. As θ_0 increases towards even larger values, a third, notably weaker, thin instability ridge appears (labelled III in figure 2a). Ridge III seems to extend all the way to $\theta_0 = 0°$, the axis of 2-D perturbations. Interestingly, ridge III becomes aligned with $\phi_0 = \Phi$ (vertical dotted lines in figure 2), indicating the emergence of shear-aligned instabilities as the ridge approaches the $\theta_0 = 0°$ axis. The existence of distinct instability bands in an otherwise stable landscape suggests the occurrence of select resonant wave–wave interactions in the small s limit, which we discuss further in §§ 3.2–3.4.

At a moderate internal wave angle, i.e. $\Phi = 45°$, as shown in figure 2(b), we similarly observe only three thin instability ridges over a (ϕ_0, θ_0)-plane that is

mostly stable. The range of 3-D wave vectors to which ridges I and II extend is smaller when compared with the case of $\Phi = 15°$ in figure 2(a). Ridge I appears to be noticeably stronger than ridge II in figure 2(b). Moreover, a third instability ridge is also identified in figure 2(b), although it is nearly indiscernible given its relatively weak growth rates. For a shallow propagating internal wave, as shown in figure 2(c) for $\Phi = 75°$, only three ridges are faintly visible due to the growth rates being an order of magnitude weaker than their $\Phi = 15°$ and $45°$ counterparts, and for the range of θ_0 to which they extend being notably limited.

For the moderate-amplitude, steep-propagation case of $(A, \Phi) = (1, 15°)$ (figure 2d), the growth rate distribution is qualitatively similar to that of figure 2(a), but with wider regions of the (ϕ_0, θ_0)-plane that are unstable. The difference between regions I and II is more dramatic than what is observed at small-amplitude (figure 2a). Moreover, region III (which was a ridge in figure 2a) contains growth rate magnitudes comparable to that of regions I and II. The larger instability regions on the (ϕ_0, θ_0)-plane imply that there is now a wider, continuous range of perturbation wave vectors whose growth rates are of comparable magnitude. At an even larger value of $A = 10$ (figure 2g), nearly the entire (ϕ_0, θ_0)-plane is unstable, with a fourth region – narrowly separated from region III – that encompasses purely transverse ($\theta_0 = 90°$) perturbations (which was not the case for weaker amplitude internal waves in figure 2a,d). As in figure 2(a), the outer boundary of region III in both figure 2(d,g) aligns with $\phi_0 = \Phi$ (shear-aligned perturbations) as $\theta_0 \to 0°$.

At a moderate-amplitude and intermediate internal wave angle, i.e. $(A, \Phi) = (1, 45°)$ (figure 2e), the instability islands cover a large part of the (ϕ_0, θ_0)-plane, but are nestled among a still sizeable region of stability. When compared with figure 2(b,e) has an additional region of instability (region IV) close to the $\theta_0 = 90°$ axis, apart from the fact that the original instability regions from $A = 0.1$ have become wider and stronger for $A = 1$. Similar to what is seen in figure 2(d,g), as A increases to 10 for $\Phi = 45°$ (see figure 2h), the entire (ϕ_0, θ_0)-plane becomes effectively unstable. Strikingly, there are at least two more separate instability regions for $A = 10$ (figure 2h) when compared with $A = 1$ (figure 2e). The largest growth rate for $(A, \Phi) = (10, 45°)$ occurs for purely transverse perturbations ($\theta_0 = 90°$). There is, however, a ridge-like feature spanning nearly all of θ_0 along $\phi_0 \approx 45°$, on which the growth rate is quite close to the maximum growth rate (which occurs on $\theta_0 = 90°$). Interestingly, the perturbation wave vectors corresponding to this near-vertical ridge are shear-aligned, i.e. $\phi_0 \approx \Phi$, in the (x, z)-plane of the base flow.

In the shallow internal wave regime of $\Phi = 75°$, the instability landscape of moderate amplitude internal waves of $A = 1$ are characterised by an array of several relatively thin unstable ridges, as shown in figure 2(f). We recall that only three instability ridges are discernible at $A = 0.1$ in figure 2(c). As the internal wave amplitude increases to $A = 10$ (figure 2i), the instability landscape changes significantly. The unstable ridges in figure 2(f) all seem to widen such that the entire (ϕ_0, θ_0)-plane, except for a small patch around $(\phi_0, \theta_0) = (75°, 0°)$, is unstable. Remarkably, there is now a vertical ridge (spanning the entire θ_0 range of $0° \leqslant \theta_0 \leqslant 90°$) at $\phi_0 = 75°$ along which the growth rate is large and nearly uniform. The overall maximum growth rate in figure 2(i) still occurs on $\theta_0 = 90°$ although the shear-aligned wave vectors on the vertical ridge are not far behind. Furthermore, at $A = 10$, the maximum growth rates at $\Phi = 75°$ are now comparable in magnitude to the growth rates at $\Phi = 45°$ and $15°$, suggesting that the dependence of maximum growth rate on Φ is weaker at larger amplitudes.

Some of the distinct instability ridges seen across Φ for $A = 1$ in figure 2(d–f) appear to be amplified extensions of the thin instability ridges observed at $A = 0.1$

in figure 2(*a–c*). For example, the first three instability regions (I, II and III) in figure 2(*d,e*) clearly have thinner, weaker counterparts in figure 2(*a,b*). Similarly, the broad and barely separated regions of instability in figure 2(*g–i*) at $A = 10$ seem to be extensions of the $A = 1$ unstable regions in figure 2(*d–f*), but not necessarily with one-to-one correspondence between scenarios of the same Φ. For example, the fourth instability region in figure 2(*g*) does not have a counterpart in figure 2(*d*). Additionally, the number of seemingly separate instability regions in figure 2(*h*) is larger than the number in figure 2(*e*). The unstable regions I–III at $\Phi = 15°$, $45°$ and $75°$ for $A = 0.1$ (in figure 2), suggest that the instabilities occurring at large A may be linked to instabilities at small A, in line with Klostermeyer (1991), who proposed a connection between small A resonances and all instability modes at all internal wave angles. Sonmor & Klaassen (1997) reaffirmed the conjecture of Klostermeyer (1991) by concluding that there exist no instabilities in finite-amplitude plane internal waves that cannot be traced back to resonant instabilities at small A. The connection between small A resonances and finite A instabilities is addressed more rigorously in §§ 3.4 and 3.5.

3.2. *Two-dimensional PSI*

In the limit of 2-D perturbations, i.e. $\theta_0 = 0°$ and small A, the local stability approach shows the existence of two distinct values of ϕ_0 at which thin instability peaks are present (figure 2*a–c*). In this section, we verify that these peaks arise from a resonant wave triad, and proceed to establish correspondence with existing results on 2-D PSI. Furthermore, the local stability approach facilitates an investigation of how 2-D PSI continuously extends towards large internal wave amplitudes as well as 3-D perturbations (we discuss the latter in § 3.3).

Resonant triad interaction (RTI) represents a mechanism by which a pair of subharmonic or superharmonic internal waves extract energy from a primary internal wave through the formation of a resonant triad (Mied 1976). Such a resonant triad is formed when the spatial and temporal resonant conditions are satisfied:

$$\boldsymbol{k}_1 + \boldsymbol{k}_2 = n\boldsymbol{k}, \tag{3.1}$$

and

$$\omega_1 + \omega_2 = n\omega, \tag{3.2}$$

where the internal wave $(\boldsymbol{k}, \omega)$ resonantly interacts with the internal waves $(\boldsymbol{k}_1, \omega_1)$ and $(\boldsymbol{k}_2, \omega_2)$, and n is any positive integer (Hasselmann 1967; Drazin 1977). In the context of RTI, $(\boldsymbol{k}, \omega)$ denote the primary wave properties presented in (2.7), the subscripts 1 and 2 denote subharmonic daughter waves and $n + 1$ is the order of the resonance. In this section and the next (§ 3.3), we will focus on second-order wave interactions, which take place for $n = 1$; higher order resonances ($n > 1$) are discussed in § 3.4.

To illustrate the main features of 2-D RTI, i.e. resonant triads formed in the plane of the primary wave, we begin by considering an arbitrary pair of daughter waves, $(\boldsymbol{k}_1, \omega_1)$ and $(\boldsymbol{k}_2, \omega_2)$, for a given primary wave $(\boldsymbol{k}, \omega)$. The conditions (3.1) and (3.2) with $n = 1$, together with the dispersion relation (2.8) for all three waves, can be solved to obtain a relation between m_1 and k_1, where $\boldsymbol{k}_1 = (k_1, 0, m_1)$ (see Bourget *et al.* 2013, equation (3.29)). A plot of m_1 (normalised by the primary vertical wavenumber m) as a function of k_1 (normalised by the primary horizontal wavenumber k) is shown in figure 3(*a*). Any point on this resonance curve describes
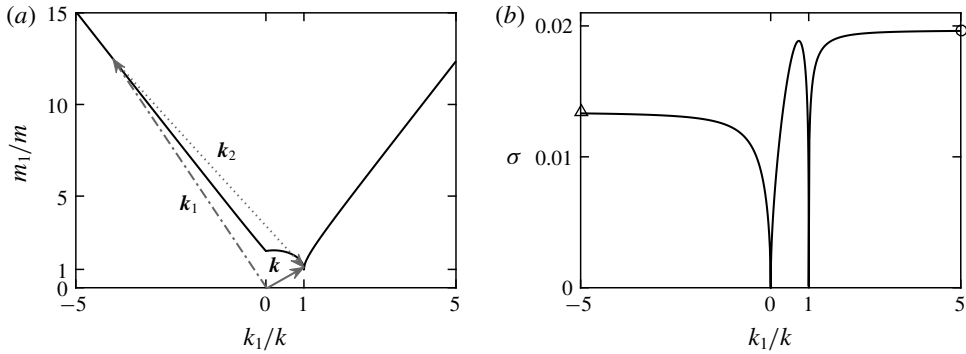
FIGURE 3. (a) The $\boldsymbol{k}_1$ resonance curve (solid black line) for a primary wave $\boldsymbol{k} = (k, 0, m)$ (depicted by the arrow starting at the origin and ending at point $(1, 1)$) obtained from the solution to the set of equations comprising the resonant conditions (3.1) and (3.2) (for $n = 1$) and the dispersion relation (2.8). Superposed onto the resonance curve is a representative PSI resonant triad: $\boldsymbol{k}$ (——), $\boldsymbol{k}_1$ (— · —), and $\boldsymbol{k}_2$ (· · ·). (b) The instability growth rates (solid line), as derived by Koudella & Staquet (2006), corresponding to the resonance curve in panel (a) for $(A, \Phi) = (0.1, 45°)$. The asymptotic values of the growth rate in the PSI limit for branch-A and branch-B (denoted by $\bigcirc$ and $\triangle$, respectively), as derived by Sonmor & Klaassen (1997), are consistent with Koudella & Staquet (2006).

the tip of $\boldsymbol{k}_1$, which when subtracted from the primary wave vector $\boldsymbol{k}$ – located at $(1, 1)$ in figure 3(a) – will yield the $\boldsymbol{k}_2$ that completes the resonant triad (Phillips 1977). An example resonant triad is presented in figure 3(a).

Of particular relevance to our study is the limit where the magnitudes of $\boldsymbol{k}_1$ and $\boldsymbol{k}_2$ are significantly larger than $\boldsymbol{k}$, which translates to short-wavelength perturbations (i.e. daughter waves) relative to the base flow (i.e. primary wave). In this limit ($|k_1| \to \infty$ and $\boldsymbol{k}_1$ lying on the resonance curve in figure 3a), $\boldsymbol{k}_1$ and $\boldsymbol{k}_2$ become increasingly anti-parallel, and both ω_1 and ω_2 approach $\omega/2$. The class of resonant triads characterised by long, anti-parallel perturbation wave vectors with frequencies that are half the primary wave frequency is referred to as PSI (McComas & Bretherton 1977; Dauxois *et al.* 2018).

Since the local stability approach and PSI both concern small-scale perturbations, we proceed to investigate the extent to which the local stability approach recovers 2-D PSI characteristics, i.e. the daughter wave vectors and associated growth rates. We focus on the case presented in figure 2(b), i.e. $(A, \Phi) = (0.1, 45°)$, which corresponds to an isopycnal steepness of $s \approx 0.07$. For 2-D perturbations ($\theta_0 = 0°$), the local stability approach identifies instabilities at $\phi_{0,1} \approx 69°$ and $\phi_{0,3} \approx 111°$, and (by virtue of the periodicity of σ with ϕ_0) at $\phi_{0,2} = \phi_{0,1} + 180°$ and $\phi_{0,4} = \phi_{0,3} + 180°$. The wave vectors $\boldsymbol{\kappa}_{0,1} = \boldsymbol{\kappa}_0(\phi_{0,1}, \theta_0 = 0°)$ and $\boldsymbol{\kappa}_{0,2} = \boldsymbol{\kappa}_0(\phi_{0,2}, \theta_0 = 0°)$, together with the base flow wave vector $\boldsymbol{k}$, satisfy the spatial triadic resonance condition (3.1) as

$$\boldsymbol{\kappa}_{0,1} + \boldsymbol{\kappa}_{0,2} = 0, \tag{3.3}$$

where $\boldsymbol{\kappa}_{0,1}$ and $\boldsymbol{\kappa}_{0,2}$ are anti-parallel to each other, and represent wave vectors of much larger magnitude than the base flow wave vector due to the short-wavelength approximation. Thus, the wave vectors $\boldsymbol{\kappa}_{0,1}$ and $\boldsymbol{\kappa}_{0,2}$ are consistent with the daughter wave vectors in the PSI limit shown in figure 3(a).

If $\kappa_{0,1}$ and $\kappa_{0,2}$ are to represent internal wave vectors, then the corresponding frequencies based on the dispersion relation should be $\omega_1/N = \cos\phi_{0,1} \approx 0.36$ and $\omega_2/N = -\cos\phi_{0,2} \approx 0.36$, both of which equal approximately half of the base flow wave frequency $\omega/N = \cos\Phi \approx 0.71$. Given that the local stability framework allows the perturbation wave vectors to evolve in time, we verify that the PSI triadic resonance conditions are satisfied over the entire time period $0 \leqslant t\cos\Phi < 2\pi$ by computing $\kappa_{0,1}(t)$ and $\kappa_{0,2}(t)$ via (2.17) and confirming them to be effectively constant in time, with $\lesssim 5\%$ variation (the variation decreases as A decreases). We have thus established that the internal waves at the unstable wave vectors $\kappa_{0,1}$ and $\kappa_{0,2}$ from the local stability approach indeed satisfy the classical PSI triadic resonance conditions with the base flow wave vector. A similar calculation reveals that the internal waves at the unstable wave vectors $\kappa_{0,3}$ and $\kappa_{0,4}$ are also in PSI triadic resonance with k. In summary, each of the two pairs of unstable 2-D perturbation wave vectors from the local stability approach represent a daughter wave pair that is in PSI resonance with k. We proceed to investigate the growth rate at these unstable wave vectors.

For small isopycnal steepness ($s \ll 1$) of the primary wave, the growth rate corresponding to any resonant triad in the plane of the primary wave is (Koudella & Staquet 2006, §4.3.1)

$$\sigma_{\mathrm{KS}} = A\cos^2\Phi\sqrt{S_1 S_2}, \tag{3.4}$$

where

$$S_p = \frac{m_r k_q - m_q k_r}{4k_3^2 |\boldsymbol{k}_p|^2}[(|\boldsymbol{k}_q|^2 - |\boldsymbol{k}_r|^2) + |\boldsymbol{k}_p|(|\boldsymbol{k}_q| - |\boldsymbol{k}_r|)]; \tag{3.5}$$

the subscripts $p, q, r = 1, 2, 3$ form a circular permutation, with 1 and 2 denoting the daughter waves and 3 denoting the primary wave.

Figure 3(*b*) shows σ_{KS} as a function of k_1/k, from which we see that the growth rate approaches two different asymptotic values at the PSI limits $k_1 \to \pm\infty$. The larger asymptote (corresponding to the maximum PSI growth rate) occurs as $k_1 \to \infty$, and is referred to as branch-A PSI. The smaller asymptote occurs in the limit $k_1 \to -\infty$, and is referred to as branch-B PSI. The growth rates in these two limits are (Sonmor & Klaassen 1997, §3):

$$\sigma_{\mathrm{SK}} = \lim_{k_1 \to \pm\infty} \sigma_{\mathrm{KS}} = \frac{A}{16}\cos\Phi[\pm 2\sin^3|\Phi| + (1 + 2\cos^2\Phi)\sqrt{4 - \cos^2\Phi}], \tag{3.6}$$

where the upper and lower signs correspond to branch-A and -B, respectively (in figure 3(*b*) we confirm that σ_{KS} approaches σ_{SK} at the PSI limits). We denote the 2-D PSI growth rates in (3.6) associated with branch-A and branch-B as σ_A and σ_B, respectively.

We find, for $(A, \Phi) = (0.1, 45°)$, the local stability growth rates to be $\sigma(\phi_{0,1}, \theta_0 = 0°) = \sigma(\phi_{0,2}, \theta_0 = 0°) = 0.01970$, which is within 0.002 % of $\sigma_A = 0.01966$. Similarly, $\sigma(\phi_{0,3}, \theta_0 = 0°) = \sigma(\phi_{0,4}, \theta_0 = 0°) = 0.01349$, which is within 0.006 % of $\sigma_B = 0.01341$. Summarising our investigations at other Φ, we conclude that the local stability approach, for small A internal waves and 2-D perturbations, recovers sharp instability peaks at $\phi_{0,1} = \cos^{-1}(\cos\Phi/2)$ and $\phi_{0,2} = \phi_{0,1} + 180°$, the growth rates at which match with that of branch-A PSI. The local stability approach also recovers sharp instability peaks at $\phi_{0,3} = \cos^{-1}(-\cos\Phi/2)$ and $\phi_{0,4} = \phi_{0,3} + 180°$, the growth rates at which match with that of branch-B PSI. We now perform a more comprehensive
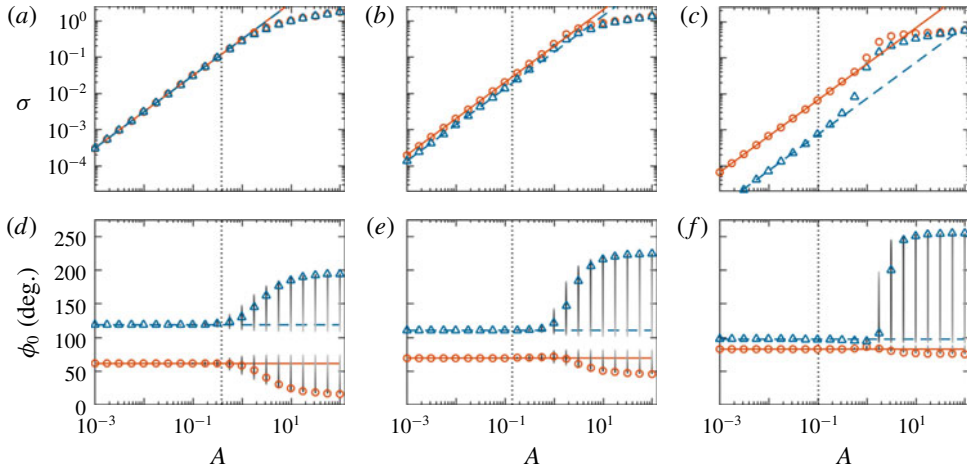
FIGURE 4. (Colour online) 2-D PSI growth rates (*a–c*) and corresponding wave vector orientations (*d–f*) presented as a function of A for $\Phi = 15°$, $45°$ and $75°$ (left, middle and right columns, respectively). The solid and dashed lines in panels (*a–c*), respectively, denote the branch-A and branch-B PSI growth rates derived by Sonmor & Klaassen (1997) in (3.6); the solid and dashed lines in panels (*d–f*) denote the corresponding perturbation wave vector orientations given by $\cos^{-1}(\pm \cos \Phi/2)$. Our local stability results are denoted by $\bigcirc$ and $\triangle$ for branch-A and branch-B PSI, respectively. The vertical lines associated with our results in panels (*d–f*) denote the width of the PSI peaks, with the colour intensity indicating the growth rates normalised by the corresponding growth rates plotted in panels (*a–c*). The value $s = 0.1$ is indicated in each panel by a dotted vertical line, indicating the upper limit of the small s regime.

comparison of 2-D PSI growth rates derived by Sonmor & Klaassen (1997) (σ_A and σ_B) and our local stability approach (σ_A^L and σ_B^L).

For a given (A, Φ), we calculate the maximum growth rate σ_A^L within the instability peak associated with $\phi_{0,1} = \cos^{-1}(\cos \Phi/2)$ for 2-D perturbations ($\theta_0 = 0°$); the corresponding location of locally maximum growth rate is denoted $\phi_{0,1}^*$, which equals $\phi_{0,1}$ only for sufficiently small A since the peaks around $\phi_{0,1}$ (and $\phi_{0,3}$) expand into finite-width instability regions as A increases. Similarly, the maximum growth rate within the instability peak around $\phi_{0,3} = \cos^{-1}(-\cos \Phi/2)$ is denoted as σ_B^L, and the corresponding location of locally maximum growth rate is $\phi_{0,3}^*$. In the top row of figure 4, we plot σ_A^L and σ_B^L as a function of A for three different internal wave orientations ($\Phi = 15°$, $45°$, and $75°$ in figure 4*a–c*, respectively). For all three Φ, there is excellent quantitative agreement between $\sigma_{A,B}^L$ (denoted by $\bigcirc$ and $\triangle$ for branch-A and -B, respectively) and the $\sigma_{A,B}$ growth rates of Sonmor & Klaassen (1997) (denoted by solid and dashed lines for branch-A and -B, respectively) for $s < 0.1$ ($s = 0.1$ is indicated by the vertical dotted lines in all panels of figure 4). The bottom row of figure 4 shows the variation of $\phi_{0,1}^*$ and $\phi_{0,3}^*$ with A, which are in excellent agreement with $\phi_{0,1}$ and $\phi_{0,3}$, respectively, for $s < 0.1$. Also shown in the bottom row of figure 4 (using vertical bars) are the widths, along ϕ_0 of the corresponding instability regions; the widths remain close to zero for $s < 0.1$ at all Φ.

As A, and thus s, increases, there is a noticeable deviation of the local stability growth rates from the PSI growth rates of Sonmor & Klaassen (1997) (top row of

figure 4). Around $s \approx 0.5$, PSI theory breaks down regardless of the specific A and Φ values. For each Φ, in the large A limit, σ_A^L and σ_B^L converge and saturate at ≈ 1, which, in dimensional time, corresponds to a growth rate of $\approx N$. In summary, branch-A PSI dominates branch-B PSI at small A, but the growth rates of both branches converge to a similar value at large A. We note that the intriguing convergence of the local stability PSI growth rates in the large A limit revealed by the local stability approach is beyond the scope of classical PSI theories. We further note that as A increases, the unstable perturbation wave vectors initialised at $\kappa_0(\phi_{0,1-4}^*, \theta_0 = 0°)$ begin to substantially evolve along the base flow fluid particle trajectories and can no longer be classified as internal waves.

For $s > 0.1$, $\phi_{0,1}^*$ and $\phi_{0,3}^*$ deviate noticeably from the branch-A and -B PSI theoretical estimates $\phi_{0,1}$ and $\phi_{0,3}$, respectively. As Φ increases, however, the deviations of $\phi_{0,1}^*$ from $\phi_{0,1}$ decrease, while the deviations of $\phi_{0,3}^*$ from $\phi_{0,3}$ increase (for $\Phi = 75°$, $\phi_{0,1}^* \approx \phi_{0,1}$ even at large A). We note that the branch-A ($\phi_{0,1}^*$) and branch-B ($\phi_{0,3}^*$) instabilities become anti-parallel to each other at large A (i.e. separated by 180°), consistent with σ_A^L and σ_B^L converging at large A. As wave steepness increases (or as A increases for fixed Φ), the branch-A peak gradually widens, although, for large Φ, the width of the peak is quite small even at large A. The width of the branch-B peak increases with A as well, with the increase being larger than that of branch-A; for $\Phi = 75°$ (figure 4f), the width of the branch-B peaks becomes very large, spanning $90° \lesssim \phi_0 \lesssim 250°$ at large A. The wider PSI peaks at large A indicate a larger range of instability, as we have seen in figure 2.

3.3. *Three-dimensional PSI*

The instability ridges for $(A, \Phi) = (0.1, 45°)$ (figure 2b), at $\theta_0 = 0°$, comprise branch-A ($\phi_{0,1} \approx 69°$ and $\phi_{0,2} = \phi_{0,1} + 180°$) and branch-B ($\phi_{0,3} \approx 111°$ and $\phi_{0,4} = \phi_{0,3} + 180°$) PSI peaks. The extension of these peaks towards 3-D perturbation wave vectors, i.e. $\theta_0 > 0°$, suggests the existence of 3-D PSI. To confirm this, we first compute σ over the (ϕ_0, θ_0)-plane for $A = 0.01$ and various values of Φ in the small s regime, and then trace the instability ridges that emerge from the $\theta_0 = 0°$ axis (figure 5a–c). The 3-D perturbation wave vectors corresponding to these traces satisfy the spatial resonant condition,

$$\kappa(\phi_0, \pm\theta_0) + \kappa(\phi_0 + 180°, \mp\theta_0) = 0, \tag{3.7}$$

along the curves in figure 5(a–c) (we recall from §2 that $\sigma(\phi_0, \theta_0) = \sigma(\phi_0 + 180°, \theta_0)$ and $\sigma(\phi_0, \pm\theta_0) = \sigma(\phi_0, \mp\theta_0)$). The equal and opposite wave vector components in y for the two daughter waves in (3.7) are a consequence of the primary wave vector $\boldsymbol{k}$ being entirely in the (x, z)-plane.

Requiring the two daughter waves in (3.7) to satisfy the 3-D internal wave dispersion relation,

$$\frac{\omega}{N} = \frac{|\boldsymbol{k}_{xy}|}{|\boldsymbol{k}|}, \tag{3.8}$$

(where $\boldsymbol{k}_{xy} = (k, \ell, 0)$ is the wave vector projected onto the xy-plane), and the temporal resonance condition in (3.2) for $n = 1$ yields the relation

$$\phi_0 = \cos^{-1}\left(\pm\sqrt{\frac{1}{4}\frac{\cos^2\Phi}{\cos^2\theta_0} - \tan^2\theta_0}\right) \quad \text{for } |\theta_0| \leqslant \sin^{-1}\left(\frac{|\cos\Phi|}{2}\right), \tag{3.9}$$
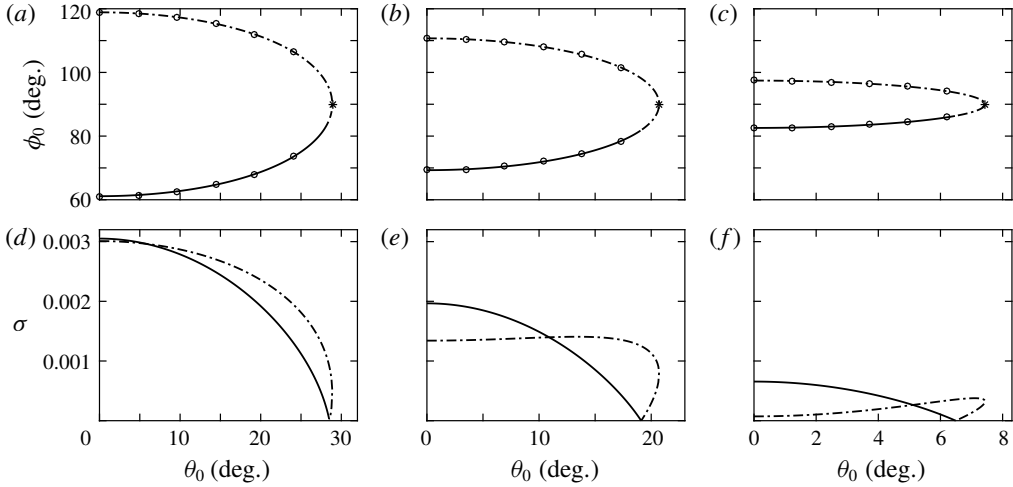
FIGURE 5. Traces of 3-D PSI ridges in the (ϕ_0, θ_0)-plane (a–c), and corresponding growth rates (d–f) for a base flow of $A = 10^{-2}$ and $\Phi = 15°$, $45°$, $75°$ (left, middle and right columns, respectively); the corresponding isopycnal steepnesses are, respectively, $s \approx 0.003$, 0.007 and 0.01. The trace segments associated with branch-A and branch-B PSI are denoted by the solid and dash-dotted lines, respectively. Superposed onto panels (a–c) are discrete points of (3.9) (denoted by the circle markers), and the threshold values of θ_0 (denoted by the asterisk markers).

with the daughter waves at frequency $\omega/2$. In figure 5(a–c), we superpose points corresponding to (3.9) onto the instability traces; the excellent agreement confirms that the temporal resonant condition is satisfied by the 3-D perturbation wave vectors that comprise each trace. Furthermore, we verify that the perturbation wave vectors on these instability traces are effectively invariant in time, with $\lesssim 1.5\%$ variation over $0 \leqslant t < 2\pi/\cos\Phi$. In summary, the perturbation wave vectors $\kappa(\phi_0, \pm\theta_0)$ and $\kappa(\phi_0 + 180°, \mp\theta_0)$ are in 3-D PSI triadic resonance with the primary wave vector k, where (ϕ_0, θ_0) is any point on the curves shown in figure 5(a–c).

Having confirmed that the instability ridges that exist at small s are indeed a 3-D manifestation of PSI, we proceed to elucidate the growth rate variation along the curves in figure 5(a–c). Each ridge has a point at which the growth rate approaches zero, which we use to separate the trace into two segments, branches-A and -B, based on which 2-D PSI branch the segment is on at $\theta_0 = 0°$ (ridges I and II in figure 2a, respectively). The growth rates corresponding to each trace are presented in figure 5(d–f). For 2-D perturbation wave vectors ($\theta_0 = 0°$), the maximum growth rate corresponds to branch-A regardless of Φ. For $\Phi = 15°$ in figure 5(d), however, branch-B is dominant for practically the entire range of $\theta_0 > 0°$. Moreover, for both $\Phi = 15°$ and $75°$ (figure 5d,f, respectively), the maximum branch-B growth rate is comparable to the maximum branch-A growth rate. Looking at 2-D PSI alone for $\Phi = 75°$, one would conclude that branch-A clearly dominates branch-B; in 3-D, however, the maximum branch-B growth rate is almost as strong as branch-A is in two dimensions.

As Φ increases, we observe five general features of 3-D PSI: (i) the range, in ϕ_0, of PSI decreases; (ii) the range, in θ_0, of branch-A (solid line in figure 5) shortens; (iii) the branch-B growth rate curve evolves from one that is monotonically

decreasing to one that increases and achieves a maximum growth rate in the vicinity of the threshold θ_0 (asterisk marker in figure 5*a–c*); (iv) the overall magnitudes of σ decrease; and (v) the threshold value of θ_0 decreases substantially, thereby restricting the three-dimensionality of the resonant wave interaction between the 3-D perturbation wave vectors and the internal wave base flow.

3.4. *Higher-order resonances*

To understand the origin of various large A instabilities, we plot, in figure 6, the growth rates in the (ϕ_0, θ_0)-plane for $\Phi = 15°$ $45°$, and $75°$ for three base flow amplitudes that reasonably span the transition from small to large A: $A = 0.3$, 0.5 and 0.7. Moreover, we superpose on figure 6 the contours along which the corresponding perturbation wave vectors are in second- or higher-order triadic resonance with the primary wave, i.e. equation (3.9) modified to include any order of resonance ($n \geqslant 1$):

$$\phi_0 = \cos^{-1}\left(\pm\sqrt{\frac{n^2}{4}\frac{\cos^2 \Phi}{\cos^2 \theta_0} - \tan^2 \theta_0}\right) \quad \text{for } |\theta_0| \leqslant \sin^{-1}\left(\frac{n}{2}|\cos \Phi|\right), \quad (3.10)$$

where the daughter waves are now at frequency $n\omega/2$. The second-order ($n = 1$) resonance contour is closest to the $\theta_0 = 0°$-axis; as n increases, the higher-order resonance curves expand outwards and approach the $\theta_0 = 90°$ axis. As Φ increases, the frequency ω/N decreases [see (2.8)], which, in turn, allows for a greater number of higher-harmonics (i.e. n) to fit within the internal wave passband $0 < n\omega/2 < N$. From (3.10), the highest possible order of resonance is specified by $n = 2$ for $\Phi = 15°$ and $45°$, and $n = 7$ for $\Phi = 75°$. Interestingly, for quasi-2-D perturbations ($\theta_0 \approx 0°$), (3.10) simplifies to $\phi_0 \approx \Phi$ (i.e. perturbations that are shear aligned) for $n = 2$ (third-order resonance). This explains the orientation of ridge III near the $\theta_0 = 0°$ axis in figure 2(*a,b*) given that ridge III corresponds to third-order resonance, as we will show below.

For $(A, \Phi) = (0.3, 15°)$ (figure 6*a*), the instability ridges are of finite width. The $n = 1$ resonance contour overlaps with its corresponding instability ridges I and II, as was reported in § 3.3. In contrast, the $n = 2$ resonance contour does not necessarily capture the most unstable locations within the corresponding instability region. Instead, the $n = 2$ contour accurately captures the upper boundary of instability region III. As A decreases, however, the instability region III of $\Phi = 15°$ becomes progressively thinner (and weaker) and overlaps with the $n = 2$ resonance contour. For $\Phi = 45°$ and $75°$ (figure 6*b,c*, respectively), the theoretical resonance curves nicely capture all of the instability ridges, although the ridges are very thin and weak for $\Phi = 75°$.

Slightly increasing A to 0.5 (figure 6*d–f*) yields results similar to $A = 0.3$. At $\Phi = 15°$, a deviation from theoretical resonance happens in the form of a widening of the instability ridges, although the signature of the higher-order resonance curves are still clearly present. The upper boundary of instability region III is still nicely captured by the $n = 2$ contour. Deviation of the instability ridges from higher-order resonance curves is notable at $\Phi = 75°$, although there is overlap near $\phi_0 = 90°$. The deviations taking place for $\Phi = 75°$ are unsurprising given that s increases with Φ, and we expect deviations to occur beyond the PSI regime for large s. Interestingly, a new instability region appears in the vicinity of the $\theta_0 = 90°$ axis for $\Phi = 45°$ (figure 6*e*), and it seems to have no corresponding theoretical resonance contour in its neighbourhood. We investigate this new instability region in § 3.5.
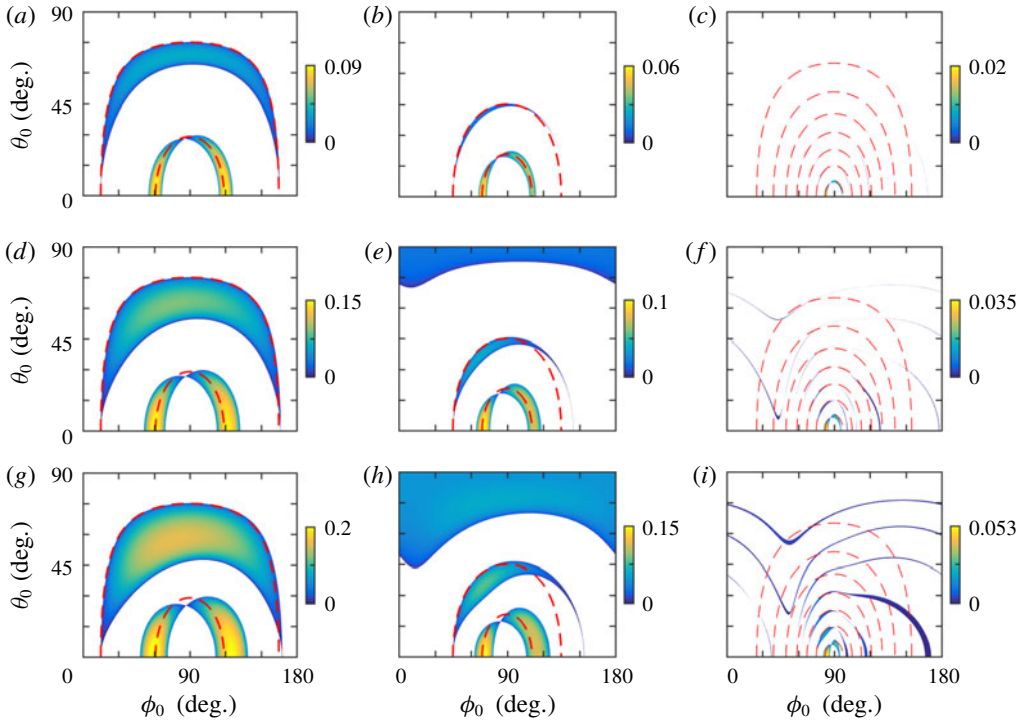
FIGURE 6. (Colour online) Growth rate, σ, in the (ϕ_0, θ_0)-plane for $\Phi = 15°$, $45°$ and $75°$ (left, middle and right columns, respectively) for $A = 0.3$, 0.5 and 0.7 (top, middle and bottom rows, respectively). Superposed onto each panel are the higher-order resonance curves (dashed lines) given by (3.10); the innermost curve corresponds to $n = 1$, with n incrementally increasing outwards. Stable regions of the (ϕ_0, θ_0)-plane where $\sigma < 10^{-10}$ have been coloured white.

The results for $A = 0.7$ depict a departure from alignment between the instability ridges and the higher-order resonance curves. Either the instability ridges widen substantially to cover a larger band of the (ϕ_0, θ_0)-plane (as for $\Phi = 15°$ and $45°$ in figure 6g,h, respectively), or they remain relatively thin but completely fall out of alignment and into a non-trivial pattern (as for $\Phi = 75°$ in figure 6i). What is most striking, however, is the connection observed between the instability ridges and the higher-order resonance curves for small A and the persistence of that connection as A increases. It appears that many features of the instability landscape, especially those corresponding to the maximum growth rates, originate from higher-order resonances in the small A regime, a result that is consistent with the conclusions of Klostermeyer (1991) and Sonmor & Klaassen (1997).

3.5. *Transverse instabilities*

In figure 6(e,h), we note the existence of an instability region near $\theta_0 = 90°$ that is seemingly independent of the higher-order resonance curves. Equation (3.10) informs us that the higher-order resonance curves approach the $\theta_0 = 90°$ axis as $\Phi \to 90°$. The appearance of the instability region at and around $\theta_0 = 90°$ for $\Phi = 45°$ (figure 6e,h), and its absence for $\Phi = 15°$ (figure 6d,g) and $75°$ (figure 6f,i), suggests that the
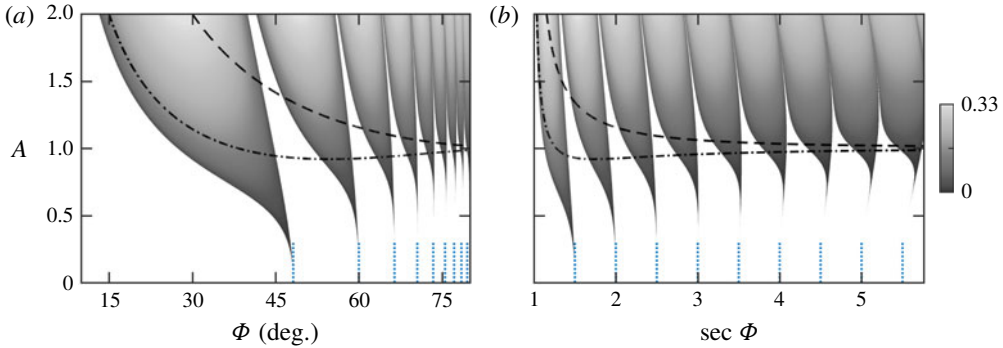
FIGURE 7. (Colour online) (a) Growth rate as a function of (A, Φ) for $\theta_0 = 90°$ (ϕ_0 is arbitrarily set to $0°$). Stable regions of the (A, Φ)-plane where $\sigma < 10^{-10}$ has been coloured white. The origin of the largest instability tongue at $A = 0$, which occurs at $\Phi_1 \approx 48°$, is marked by the left-most vertical dotted line. Additional tongues occur at half-integer multiples of $\sec \Phi_1$, as shown in panel (b). The threshold for gravitational stability, (3.14), is denoted by the dashed line, and the modified gravitational stability threshold, (3.15), is denoted by the dash-dotted line.

transverse $\theta_0 = 90°$ instability is unrelated to higher-order resonances. We note that the perturbation wave vector giving rise to the purely transverse instability is normal to the plane of the base flow, and thus invariant in time [by virtue of (2.12)].

To better understand this transverse instability, we plot the growth rate for $\theta_0 = 90°$ (and ϕ_0 arbitrarily set to $0°$) as a function of (A, Φ) in figure 7. Interestingly, there are distinct instability tongues spanning the (A, Φ)-plane. These tongues seem to originate at specific points along the Φ-axis at $A = 0$, where the growth rates are infinitesimal. Substituting purely transverse perturbations ($\kappa_0 = \hat{e}_y$) into equations (2.13) and (2.14) yields a set of coupled ordinary differential equations for a_x and a_z:

$$\frac{\mathrm{d}^2 a_x}{\mathrm{d}t^2} + A \cos^2 \Phi \sin \Phi \sin(\vartheta_0 - \cos \Phi t) a_x$$
$$= -A \sin^2 \Phi \cos \Phi \sin(\vartheta_0 - \cos \Phi t) a_z$$
$$\quad - A \sin \Phi \cos(\vartheta_0 - \cos \Phi t) \left(\cos \Phi \frac{\mathrm{d}a_x}{\mathrm{d}t} + \sin \Phi \frac{\mathrm{d}a_z}{\mathrm{d}t} \right), \qquad (3.11)$$

$$\frac{\mathrm{d}^2 a_z}{\mathrm{d}t^2} + [1 - A \sin \Phi (1 + \cos^2 \Phi) \sin(\vartheta_0 - \cos \Phi t)] a_z$$
$$= A(\cos^3 \Phi + \cos \Phi) \sin(\vartheta_0 - \cos \Phi t) a_x$$
$$\quad + A \cos \Phi \cos(\vartheta_0 - \cos \Phi t) \left(\cos \Phi \frac{\mathrm{d}a_x}{\mathrm{d}t} + \sin \Phi \frac{\mathrm{d}a_z}{\mathrm{d}t} \right). \qquad (3.12)$$

After neglecting the forcing and damping terms on the right-hand side of (3.12), we obtain a Mathieu-like equation for a_z which describes a parametrically forced system that has instability tongues in the (A, Φ)-plane corresponding to regions of parametric resonance. These tongues originate at $A = 0$ from the following points (Bender & Orszag 1999, chap. 11.4):

$$\Phi = \cos^{-1} \left(\frac{2}{n+2} \right), \quad n = 1, 2, 3, \ldots. \qquad (3.13)$$

The points given by (3.13), which are denoted by vertical dotted lines in figure 7, accurately predict the points along the Φ-axis from which the tongues emanate. As A increases, the points widen into instability regions with finite and increasing growth rates. We do observe, however, a detachment of the tongues (especially for large Φ) from the $A = 0$ axis, which we attribute to the damping and forcing terms in the right-hand side of (3.11) and (3.12) (Nayfeh & Mook 1995, chap. 1.5).

The first tongue originating at $\Phi_1 \approx 48°$ spans the largest region of the (A, Φ)-plane, and the bulk of the tongue appears to take form at relatively smaller values of A. It is this tongue that we observe in figure 6(e) at $(A, \Phi) = (0.5, 45°)$; the other tongues at larger Φ have not taken form by $A = 0.5$, which explains the absence of a transverse instability in figure 6(f) at $\Phi = 75°$. We note that it is the peculiar shape of the instability tongues (the inclined upper boundary in particular) that accounts for $(A, \Phi) = (1, 45°)$ having no purely transverse instabilities (figure 2e), in contrast to smaller $A = 0.5$ and 0.7 for $\Phi = 45°$ (figure 6e,h) having purely transverse instabilities. Another consequence of the non-trivial formation of transverse instabilities is region IV in figure 2(e). Although it has detached from the $\theta_0 = 90°$ axis, region IV is an extension of the transverse instability seen at smaller A in figure 6(h). (For $\Phi = 45°$, we observe the detachment of region IV from the $\theta_0 = 90°$ axis at some A in $0.95 < A < 0.96$.)

The density of tongues grows as $\Phi \to 90°$ and remapping the growth rates to the $(A, \sec \Phi)$-plane better reveals the formation of instability tongues (figure 7b). We superpose on each plot in figure 7 the threshold amplitude below which statically unstable layers do not occur at any time during the internal wave period:

$$\max_{0 \leqslant t < 2\pi/\cos\Phi} \left(\frac{\mathrm{d}\bar{\bar{\rho}}}{\mathrm{d}z} + \frac{\partial\bar{\rho}}{\partial z} \right) < 0, \quad \text{or} \quad A < \frac{1}{\sin\Phi}, \tag{3.14a,b}$$

where $\bar{\bar{\rho}}(z)$ is the background density stratification and $\bar{\rho}(\boldsymbol{x}, t)$ is the density field of the internal wave base flow. The minimum A at which the instability tongues form increases with Φ and appears to approach the gravitational stability curve (dashed line in figure 7) at large Φ. The region above the gravitational stability curve is largely unstable, although thin bands of stability separate the unstable tongues.

Without parametric pumping (i.e. the time dependency in the coefficient of a_z), equation (3.12), with the right-hand side set to zero, would have neutrally stable oscillatory solutions if

$$A < \frac{1}{\sin\Phi(1 + \cos^2\Phi)}, \tag{3.15}$$

which appears to be a slightly modified version of the static gravitational stability criterion (3.14). The inclusion of parametric pumping, however, allows for unstable solutions (i.e. parametric resonance) – even if the coefficient of a_z is positive over the entirety of the forcing period – provided that the pumping occurs at half-integer multiples of the natural period of the system (3.13). In an effort to separate the influence of parametric pumping on wave stability, we identify, in (3.15), a heuristic measure of stability by requiring the coefficient of a_z in (3.12) to be positive at all times. The criterion in (3.15), which is plotted as a dash-dotted curve in figure 7, adequately separates the bulk of the instability tongues from the stems connecting them to $A = 0$. The region above (3.15) in figure 7 is overwhelmingly unstable due to both parametric and gravitational-like instability given that the coefficient of a_z in

the left-hand side of (3.12) is negative for a substantial portion of the wave period; the thin instability stems below (3.15) exist entirely due to parametric resonance.

Although the transverse instability regions and other instability ridges seen in figure 6 both originate at small A, the former arises from parametric resonance and the latter from RTI. The instabilities associated with transverse perturbations, therefore, offer another mechanism, separate from RTI, by which large A instabilities can form. Our findings remain in line with the position of Klostermeyer (1991) and Sonmor & Klaassen (1997), who conclude that all large A instabilities are linked to small A resonances.

3.6. *Dominant instability modes*

To identify the dominant instability mode for a given (A, Φ), we calculate σ over the entire (ϕ_0, θ_0)-plane and then select the maximum growth rate, which we denote σ^*. The corresponding ϕ_0 and θ_0 of σ^*, denoted ϕ_0^* and θ_0^*, respectively, reflect the initial wave vector orientation of the most unstable perturbation. Figures 8(*a*)–8(*c*), respectively, plot σ^*, θ_0^* and ϕ_0^* over a range of base flow parameters (A, Φ). Moreover, we derive from figure 8 a regime diagram for the various dominant instability modes, which we present in figure 9. We superpose on each plot in figures 8 and 9 the boundary below which the gravitational stability criterion given by (3.14) is satisfied (dashed line), and the boundary below which the classical shear stability criterion is satisfied (dotted line):

$$\min_{0 \leqslant t < 2\pi / \cos \Phi} Ri > \frac{1}{4} \quad \text{or} \quad A < \frac{2}{\sin^2 \Phi}, \qquad (3.16a,b)$$

where $Ri = N^2/(\mathrm{d}\bar{u}/\mathrm{d}z)^2$ is the instantaneous Richardson number associated with the base flow without accounting for the unsteady density gradients associated with the internal wave. We note that (3.14) represents the stability criterion for a steady, one-dimensional (1-D), vertical density gradient with no shear flow; similarly, (3.16) is strictly valid only for 1-D shear and density profiles along the direction of gravity. Despite their limitations, (3.14) and (3.16) do provide points of reference for evaluating the relevance of classical gravitational and shear instability criteria to the emergence of various instabilities in the local stability approach. Interestingly, if we include the unsteady density gradients associated with the internal wave base flow in the definition of the Richardson number, i.e. $Ri = (N^2 - (g/\rho_0)\,\mathrm{d}\bar{\rho}/\mathrm{d}z)/(\mathrm{d}\bar{u}/\mathrm{d}z)^2$, then the boundary given by $\min_{0 \leqslant t < 2\pi / \cos \Phi} Ri > 1/4$ coincides with the gravitational stability boundary in (3.14).

In general, σ^* monotonically increases with A for a given Φ. For a given A, however, σ^* decreases with Φ for $A \ll 10$ because the dominant instability in that regime is PSI (as discussed below and shown in figure 9), for which we know that σ_A decreases with Φ (as shown in figure 4*a*–*c*). For $A \gtrsim 10$, σ^* decreases with Φ below some Φ value, past which σ^* abruptly begins to increase. This dual-behaviour of σ^* for $A \gtrsim 10$ is linked to a transition of the dominant instability mode, as discussed later in this section.

The corresponding θ_0^* values, shown in figure 8(*b*), clearly indicate a number of distinct regimes of the dominant instability mode. Up to $A \sim 1$, the dominant instability is 2-D by virtue of the perturbation wave vectors having $\theta_0 = 0°$. As we have shown in §3.2, the dominant instability mode for small A and 2-D perturbations is 2-D PSI. As further evidence, we note that the corresponding ϕ_0^* values in this regime (shown
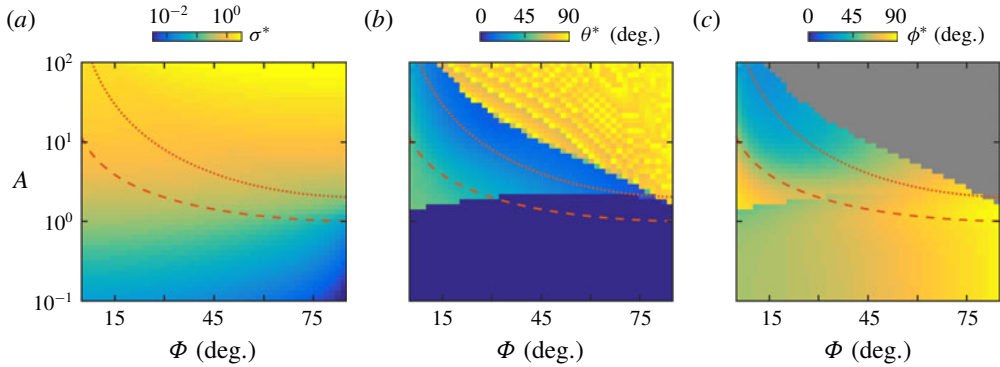
FIGURE 8. (Colour online) (*a*) Maximum growth rate, σ^*, as a function of A and Φ, and the corresponding perturbation wave vector orientations (*b*) θ_0^* and (*c*) ϕ_0^*. The dashed $(--)$ and dotted $(\cdots)$ lines denote threshold boundaries of gravitational and shear stability, respectively.
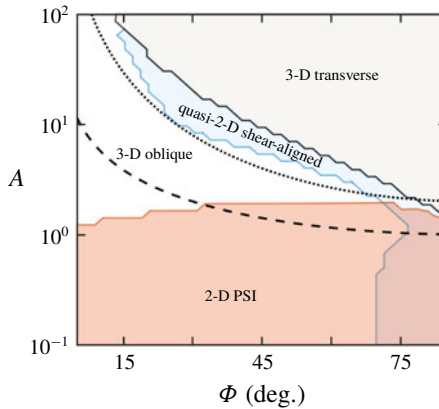

FIGURE 9. (Colour online) Regime diagram indicating the dependence of the dominant instability mode on the base flow orientation, Φ, and amplitude, A. The thresholds for gravitational and shear stability are denoted by the dashed $(--)$ and dotted $(\cdots)$ lines, respectively.

in figure 8*c*) are independent of A and approach $90°$ as Φ increases, both of which are in agreement with the behaviour of branch-A PSI in figure 4(*d*–*f*). The boundary for classical shear stability (dotted line in figures 8 and 9) appears to nicely delineate this limit of the PSI regime for sufficiently large Φ.

Beyond the upper boundary of the 2-D PSI regime, there is another distinct regime where θ_0^* is close to $90°$ (figure 8*b*), which corresponds to a dominant mode that is transverse to the base flow. This 3-D instability dominates for large A, with the threshold in A decreasing as $\Phi \to 90°$. We note that there are only certain points in this regime where θ_0^* is precisely $90°$; the mean and standard deviation of θ_0^* are approximately $81°$ and $6.5°$, respectively. In figure 7, we see that the instability tongues for purely transverse perturbations are separated by thin stability bands along the Φ axis at large A. The transverse dominant instability mode may, therefore, be slightly offset from $\theta_0^* = 90°$, as we see in figure 8(*b*), due to the presence of these

thin stability bands. Despite transverse perturbations having the maximum growth rate in the (ϕ_0, θ_0)-plane at large A, we recall that there are instabilities spanning nearly the entire range of θ_0 at $\phi_0^* \approx \Phi$ with growth rates close to σ^* (see, for example, figure 2*i*).

Sandwiched between the distinct 3-D transverse and 2-D PSI regimes are two intermediary regimes: one where the dominant perturbation wave vector is effectively 2-D and shear-aligned, and another regime where the perturbation wave vector is 3-D over a range of oblique angles. We identify the shear-aligned regime as one where ϕ_0^* is within 15° of Φ and is thus aligned with the direction of shear in the base flow. Moreover, the corresponding θ_0^* values are all less than 15°, which translates to perturbation wave vectors that are effectively two-dimensional. From figures 8(*c*) and 9, we can see that the shear-aligned regime hugs the lower boundary of the 3-D transverse regime and, for small A and large Φ, overlaps with the 2-D PSI regime. The overlap of the shear-aligned and 2-D PSI regimes is to be expected since the ϕ_0 values for branch-A PSI approach 90° as $\Phi \rightarrow 90°$ (as can be seen in figure 4*d–f*). The lower boundary of the non-PSI shear-aligned regime is nicely captured by the shear stability curve, as shown in figure 9.

The classical shear stability curve nicely separates the shear-aligned regime from the remaining regime, which is located below the shear stability curve and above the 2-D PSI regime. This regime corresponds to perturbation wave vectors with oblique 3-D θ_0^* ($40° \lesssim \theta_0^* \lesssim 50°$) and a range of ϕ_0^* that is strongly dependent on A and Φ. Interestingly, this 3-D oblique regime is situated between two regimes that are predominantly two-dimensional.

Figure 9 presents a summary diagram of the four dominant instability regimes (listed in increasing A): 2-D PSI, 3-D oblique, quasi-2-D shear-aligned, and 3-D transverse (with the quasi-2-D shear-aligned and 2-D PSI regimes overlapping for $\Phi > 70°$). The shear stability curve separates the 2-D PSI and 3-D oblique regimes from the quasi-2-D shear-aligned and 3-D transverse regimes. Given how our calculations are restricted to small-scale instabilities, it is only our 2-D branch-A PSI regime, at small A, that is in agreement with the dominant instability regime diagram of Sonmor & Klaassen (1997, figure 22); both of our studies also recover a shear-aligned regime, but the shear-aligned regime of Sonmor & Klaassen (1997) overlaps with our 3-D transverse regime in the (A, Φ)-plane. A more quantitative comparison of the other regimes in figure 22 of Sonmor & Klaassen (1997) are precluded because they are derived from finite-scale instabilities, which are beyond the scope of the local stability approach.

4. Geophysical application

To estimate the instability regimes in which oceanic internal waves could lie, we consider parameter values that are representative of the region around the Kaena ridge near the Hawaiian islands, known to be a location for enhanced internal tide generation (Rudnick *et al.* 2003).

Internal tides occur predominantly at the semi-diurnal frequency of $\omega \approx 1.4 \times 10^{-4}$ rad s^{-1}, and a typical stratification profile in the region shows a value of $N \approx 7.6 \times 10^{-4}$ rad s^{-1} in the deep ocean, where the stratification is effectively uniform (Echeverri & Peacock 2010). Neglecting background rotation, these values of ω and N correspond to $\Phi \approx 79.4°$ (2.8) in the deep ocean. For a given barotropic velocity amplitude U, linear models of internal tide generation at the Kaena ridge predict that the internal tide horizontal velocities are of the order of $10U$ and the

horizontal length-scale of the internal tides are ≈ 25 km (Echeverri & Peacock 2010; Mathur, Carter & Peacock 2016). Assuming $U \approx 2$ cm s^{-1}, a resulting estimate for A is 0.37 (2.9). We note, however, that the uncertainties in U and the length scale of the internal tides introduce significant uncertainty into our estimate for A.

For values of (A, Φ) around $(0.37, 79.4°)$, figure 9 identifies the dominant instability mode to be 2-D PSI, with the growth rate distribution on the (ϕ_0, θ_0)-plane resembling the instability ridges shown in figure 6(c). From figure 8(a), we find the corresponding maximum growth rate to be approximately 0.017, which is $\approx 10\%$ of the internal wave frequency $\cos \Phi$, i.e. the rate of energy extraction from the primary plane wave could occur on a time scale that is ≈ 10 times longer than the internal tide time period. Moreover, for values of Φ as large as $79.4°$, a number of higher-order resonances are possible (as shown in figure 6(c,f) for $\Phi = 75°$), which have finite growth rates that can possibly give rise to further redistribution of internal wave energy. We note that, apart from the uncertainties in the estimate of A and Φ, the exclusion of background rotation from our calculations could also affect the accuracy of our conclusions regarding the Kaena ridge. Nonetheless, the identification of 2-D PSI as the dominant instability mode is consistent with the observations of Alford *et al.* (2007) near the Hawaiian ridge.

Viscous effects, which have thus far been absent in our study, are likely to have an effect on the local instabilities. Assuming weak viscous effects, i.e. $\nu \sim O(\varepsilon^2)$ [where ν is the kinematic viscosity and ε is the short-wavelength parameter introduced in (2.11)], the viscous correction to the inviscid growth rates is given by (Landman & Saffman 1987):

$$\frac{\nu}{T} \int_0^T |\boldsymbol{\kappa}|^2 \, \mathrm{d}t, \tag{4.1}$$

where T is the time period of the fluid particle trajectory on which the local stability equations are solved. In non-dimensional terms, ν would be replaced by the inverse of the appropriately defined Reynolds number, which in our study is $Re = N/(\nu |\boldsymbol{k}|^2)$.

We assume an initial perturbation wave vector of the form in (2.16), but with its magnitude κ_0 not necessarily restricted to unity. Using the closed form expression in (2.17) for the evolution of $\boldsymbol{\kappa}$, the viscous correction to the inviscid growth rate is analytically evaluated to give

$$\sigma_\nu = \sigma - \tilde{\kappa}_0^2 \frac{\nu}{N} \left[1 + \frac{A^2}{2} \frac{\cos^2 \theta_0}{\cos^2 \Phi} \sin^2(\Phi - \phi_0) \right], \tag{4.2}$$

where σ_ν is the viscous growth rate, σ is the numerically calculated inviscid local instability growth rate and $\tilde{\kappa}_0 = |\boldsymbol{k}| \kappa_0$ is the dimensional magnitude of the initial perturbation wave vector. We recall that σ and σ_ν are non-dimensional, with N^{-1} used as the time scale.

Using the expression in (4.2), we write the threshold wavenumber

$$\tilde{\kappa}_0^T = \sqrt{\frac{\sigma N}{\nu} \left[1 + \frac{A^2}{2} \frac{\cos^2 \theta_0}{\cos^2 \Phi} \sin^2(\Phi - \phi_0) \right]^{-1}}, \tag{4.3}$$

above which viscous effects completely suppress the inviscid instability of growth rate σ. Correspondingly, $\tilde{\lambda}_0 = 2\pi/\tilde{\kappa}_0$ is the shortest dimensional wavelength for which viscous effects do not completely suppress the inviscid instability; the horizontal and

vertical wavelengths are $\tilde{\lambda}_{0,x} = 2\pi/(\tilde{\kappa}_0|\cos\theta_0\cos\phi_0|)$ and $\tilde{\lambda}_{0,z} = 2\pi/(\tilde{\kappa}_0|\cos\theta_0\sin\phi_0|)$. Interestingly, (4.3) simplifies to $\tilde{\kappa}_0^T = \sqrt{\sigma N/\nu}$ in the limit of either $\theta_0 = 90°$ (purely transverse perturbations) or $\phi_0 = \Phi$ (shear-aligned perturbations).

As discussed earlier in this section, $(A, \Phi) \approx (0.37, 79.4°)$ in the Kaena ridge region and the resulting maximum $\sigma \approx 0.017$ occurs at $(\phi_0^*, \theta_0^*) \approx (85.1°, 0°)$. These values, along with $N \approx 7.6 \times 10^{-4}$ rad s^{-1} and $\nu = 10^{-6}$ m^2 s^{-1}, are substituted into (4.3) to give $\tilde{\lambda}_0 \approx 1.8$ m, $\tilde{\lambda}_{0,x} \approx 20.7$ m, $\tilde{\lambda}_{0,z} \approx 1.8$ m, suggesting that the small-scale instability predicted by the local stability framework would indeed occur for short-wavelength perturbations since the internal tide length scales are at least an order of magnitude larger than these cut-off wavelengths. Even if the effective kinematic viscosity is increased to $\nu \sim 10^{-4}$ m^2 s^{-1} (by small-scale turbulence, for example), the cut-off wavelengths only increase by a factor of 10 and still remain relatively small. For $(A, \Phi) \approx (0.37, 79.4°)$, there is also a local maximum of $\sigma \approx 0.01$ at $(\phi_0, \theta_0) \approx (91.3°, 5°)$. With $N = 7.6 \times 10^{-4}$ rad s^{-1} and $\nu = 10^{-6}$ m^2 s^{-1}, the cut-off wavelengths are $\tilde{\lambda}_0 \approx 2.4$ m, $\tilde{\lambda}_{0,x} \approx 105$ m and $\tilde{\lambda}_{0,z} \approx 2.4$ m. Again, with an enhanced effective diffusivity of $\nu = 10^{-4}$ m^2 s^{-1}, these cut-off wavelengths increase by a factor of 10 and are still well below internal tide length scales. While viscous effects would suppress the inviscid instabilities at sufficiently small perturbation length scales, it seems unlikely that they would significantly affect the dominant local instabilities under typical oceanic conditions of strong internal tide generation.

5. Summary and conclusions

We have applied the local stability approach to gain insights into 3-D, small-scale, linear instabilities of plane internal gravity waves. The short-wavelength approximation reduces the linearised perturbation equations to a set of ordinary differential equations governing the evolution of the perturbation wave vector and leading-order perturbation amplitude along fluid particle trajectories in the plane internal wave. The resulting local stability equations are computationally inexpensive to solve, and hence allow us to obtain detailed plots of growth rates as a function of the coordinates characterising the initial perturbation wave vector, (ϕ_0, θ_0). We subsequently extend our calculations to a continuous range of (A, Φ), parameters which, respectively, characterise the amplitude and orientation of the plane internal wave. It is noteworthy that the extent to which the local stability approach recovers existing knowledge of plane internal wave instabilities was *a priori* unknown. An important outcome of this paper is, therefore, the demonstration of quantitative agreement between the local and global stability approaches (in the appropriate limit of small-scale perturbations) for a plane internal wave.

Small A internal waves are characterised by thin instability ridges in the (ϕ_0, θ_0)-plane. The number of such ridges seemed to generally increase with Φ, i.e. shallow internal waves correspond to the presence of more instability ridges. At moderate A, the weak, thin instability ridges from small A evolve into stronger, wider instability regions. For a given Φ, we also observe newer instability regions emerge in the neighbourhood of purely transverse perturbations at moderate A. At sufficiently large A, purely transverse instability seems to become dominant at all Φ, although shear-aligned perturbations spanning some or all of θ_0 are not far behind in growth rate. For small A and 2-D perturbations, we showed that the two instability ridges recover the well-known PSI branch-A and -B characteristics, including both the secondary wave vectors and the growth rate magnitudes; at sufficiently large A, the growth rates of the two PSI branches become equally strong, and the ridges

become significantly wider in the range of unstable wave vectors. It is noteworthy that the local stability approach requires no additional assumptions to capture the large amplitude extension of 2-D PSI. Three-dimensional manifestations of branch-A and branch-B PSI were then highlighted, an aspect that is potentially important in the ocean and the atmosphere. At small A, while branch-A 2-D PSI is dominant, we showed that the 3-D extension of both branch-A and -B may have similar growth rates; for branch-B, the 3-D perturbations are sometimes more unstable than their 2-D counterparts.

We then proceeded to show that the remaining unstable ridges in the (ϕ_0, θ_0)-plane for small A are also manifestations of unstable resonant triads, but of higher-order RTI. The PSI and higher-order resonances at small A were shown to continuously evolve into complex instability regions in the (ϕ_0, θ_0)-plane at moderate and large A. A notable exception was an instability region encompassing (or located close to) the axis of purely transverse perturbations ($\theta_0 = 90°$), which had no apparent connection to triadic resonance of any order. A detailed investigation of purely transverse instabilities showed that a parametric resonance mechanism results in instabilities at specific Φ at small A. The parametric resonance regions were then shown to expand into instability tongues as A increased, nearly occupying the entire range of Φ for $A > 2$. A modified form of the classical gravitational instability criterion was then shown to accurately capture the threshold amplitude above which the transverse instability regions encompass large portions of the (A, Φ)-plane.

Subsequently, we investigated the dominant instability for any (A, Φ), although our earlier results suggest that an identification of a unique dominant instability mode may potentially ignore, particularly at large A, several other perturbation wave vectors that have quantitatively similar growth rates to the dominant instability. The local stability approach identifies four distinct dominant instability regimes in the (A, Φ)-plane: 2-D PSI, 3-D oblique, quasi-2-D shear-aligned and 3-D transverse.

The relevance of classical gravitational instability (i.e. the appearance of statically unstable layers) and shear instability ($Ri < 1/4$) were then addressed by plotting the corresponding curves in the (A, Φ)-plane of the dominant instability mode regime diagram. The gravitational instability criterion reasonably serves the purpose of identifying when 2-D PSI ceases to be the dominant instability mode, except for steep internal waves. Similarly, the classical shear instability criterion seems to somewhat delineate the regions of 3-D oblique and quasi-2-D shear-aligned dominant instabilities. For any given Φ, at sufficiently large A, a transverse instability that arises from a combination of parametric resonance and gravitational-like instability becomes dominant, although non-transverse shear-aligned perturbations are strongly unstable as well. In summary, while the classical instability criteria based on idealized, 1-D base flow profiles have some role in understanding the regions of various instability mechanisms, the use of $Ri < 1/4$ criterion as a signature of turbulence in an internal wave dominated flow field represents an over simplification. In actuality, the scope of 3-D small-scale instabilities in an internal wave field is rather complex, as demonstrated by figure 9. The fact that flows in the ocean and atmosphere are by nature three-dimensional further underscores the importance of understanding the behaviour of 3-D instabilities. Typical values of oceanic parameters from the Kaena ridge suggest that 2-D PSI may be dominant, but is present alongside other 3-D instabilities. We conclude by quantitatively estimating the role of weak viscous effects in suppressing the inviscid instabilities derived from the local stability framework.

Typical studies concerning the estimation of RTI characteristics involve a two-step procedure: (i) the identification of all wave vectors that are in triadic resonance

with a given primary wave field and (ii) the derivation of evolution equations (based on weakly nonlinear expansions) that are then solved by analytical or numerical means. In a uniform stratification, the identification of all possible resonant triads that contain the primary wave involves simultaneously solving the spatial and temporal resonance conditions, along with the dispersion relation for the secondary waves. In a non-uniform stratification, however, even the identification of resonant triads for a plane wave or mode is in itself a complex task (e.g. Varma & Mathur 2017) since there is no unique vertical wavenumber associated with the wave field, contrary to the case of a plane wave or mode in a uniform stratification. Moreover, theoretical studies are often restricted to specific resonant triads, like 2-D PSI (where the daughter waves have half the primary wave frequency), which imposes the dominant instability mechanism in the problem formulation. Even if the dominant resonant triad is correctly selected for the problem at hand, we have shown that the most-unstable perturbation wave vectors are not necessarily in exact triadic resonance with the primary wave, but offset from theoretical RTI contours.

The local stability approach circumvents the two-step procedure described in the previous paragraph and instead provides a direct growth rate estimate associated with all possible perturbation wave vectors for a given base flow internal wave; the approach is not necessarily restricted to perturbations that are in triadic resonance with the primary wave. The Floquet solution form used by Mied (1976) and Sonmor & Klaassen (1997) does achieve the same goal of providing growth rate estimates for all perturbation wave vectors, but it is restricted to spatially and temporally periodic primary wave fields. It is possible, however, to account for spatial non-periodicity in the Floquet solution by methods discussed by Kataoka & Akylas (2013, § 2), albeit at significantly higher computational cost than for spatially periodic waves. Unless additional assumptions are made, like long-wavelength perturbations in Kataoka & Akylas (2013), the Floquet problem requires an infinite series be truncated to a finite number of modes. In contrast to Floquet theory, the local stability approach is computationally efficient – even for large-amplitude internal waves and 3-D perturbations – and does not require spatial periodicity of the primary wave field. Local stability may, therefore, offer an alternative approach to interpreting both resonant and non-resonant instabilities in various settings studied by laboratory experiments, numerical simulations and field studies. In fact, the local stability approach could even identify specific regions conducive to instabilities in a spatially non-uniform internal wave field. For example, the generation of higher harmonics or subharmonics when an internal wave beam impinges on a pycnocline (Mercier *et al.* 2012; Gayen & Sarkar 2013) can be the result of an instability on the underlying linear wave field.

The local stability approach does have its limits, however. Our study is restricted to short-wavelength perturbations of an internal wave, which is a reasonable assumption for geophysical flows, but not so for laboratory experiments. Moreover, the local stability approach requires periodic particle trajectories and wave vectors; the relevance of non-periodic fluid particle trajectories and wave vectors remains largely unexplored. Even for periodic wave vectors, the physical interpretation of an evolving, non-constant wave vector along the fluid particle trajectories, and hence the construction of an equivalent global eigenmode, remains unclear. Finally, the incorporation of finite-wavenumber effects (Bayly 1986) in the local stability approach remains an important step in making it more representative of realistic settings and establishing a connection with the global stability approach.

A natural extension of our study would be to incorporate the effects of background rotation. One could also investigate if the local stability approach recovers, and

provides additional insight into, the instabilities that are attributed to the finite-width feature of internal wave beams (Karimi & Akylas 2014; Dauxois *et al.* 2018). It would also be worthwhile to consider the effects of background shear and individual or combinations of internal wave modes. Finally, the local stability approach may motivate targeted 3-D direct numerical simulations to investigate the actual path towards turbulence, dissipation and mixing depending on the dominant linear instability mode.

Acknowledgements

REFERENCES

ALFORD, M. H., MACKINNON, J. A., ZHAO, Z., PINKEL, R., KLYMAK, J. & PEACOCK, T. 2007 Internal waves across the Pacific. *Geophys. Res. Lett.* **34**, L24601.

ARAVIND, H. M., MATHUR, M. & DUBOS, T. 2017 Short-wavelength secondary instabilities in homogeneous and stably stratified shear flows. arXiv:1712.05868v2.

BAYLY, B. J. 1986 Three-dimensional instability of elliptical flow. *Phys. Rev. Lett.* **57**, 2160–2163.

BAYLY, B. J., HOLM, D. D. & LIFSCHITZ, A. 1996 Three-dimensional stability of elliptical vortex columns in external strain flows. *Phil. Trans. R. Soc. Lond.* A **354**, 895–926.

BENDER, C. M. & ORSZAG, S. A. 1999 *Advanced Mathematical Methods for Scientists and Engineers*. Springer.

BOURGET, B., DAUXOIS, T., JOUBAUD, S. & ODIER, P. 2013 Experimental study of parametric subharmonic instability for internal plane waves. *J. Fluid Mech.* **723**, 1–20.

CHICONE, C. 2000 *Ordinary Differential Equations with Applications*. Springer.

CONSTANTIN, A. & GERMAIN, P. 2013 Instability of some equatorially trapped waves. *J. Geophys. Res.: Oceans* **118**, 2802–2810.

DAUXOIS, T., JOUBAUD, S., ODIER, P. & VENAILLE, A. 2018 Instabilities of internal gravity wave beams. *Annu. Rev. Fluid Mech.* **50**, 1–28.

DRAZIN, P. G. 1977 On the instability of an internal gravity wave. *Proc. R. Soc. Lond.* A **356**, 411–432.

ECHEVERRI, P. & PEACOCK, T. 2010 Internal tide generation by arbitrary two-dimensional topography. *J. Fluid Mech.* **659**, 247–266.

FRITTS, D. C. & YUAN, L. 1989 An analysis of gravity wave ducting in the atmosphere: Eckart's resonances in thermal and Doppler ducts. *J. Geophys. Res.* **94**, 18455–18466.

GALLAIRE, F., MARQUILLIE, M. & EHRENSTEIN, U. 2007 Three-dimensional transverse instabilities in detached boundary layers. *J. Fluid Mech.* **571**, 221–233.

GARRETT, C. & MUNK, W. 1975 Space-time scales of internal waves: a progress report. *J. Geophys. Res.* **80**, 291–297.

GAYEN, B. & SARKAR, S. 2013 Degradation of an internal wave beam by parametric subharmonic instability in an upper ocean pycnocline. *J. Geophys. Res.: Oceans* **118**, 4689–4698.

GODEFERD, F. S., CAMBON, C. & LEBLANC, S. 2001 Zonal approach to centrifugal, elliptic and hyperbolic instabilities in Stuart vortices with external rotation. *J. Fluid Mech.* **449**, 1–37.

HASSELMANN, K. 1967 A criterion for nonlinear wave stability. *J. Fluid Mech.* **30**, 737–739.

HINES, C. O. 1971 Generalizations of the Richardson criterion for the onset of atmospheric turbulence. *Q. J. R. Meteorol. Soc.* **97**, 429–439.

IONESCU-KRUSE, D. 2014 Instability of edge waves along a sloping beach. *J. Differ. Equ.* **256**, 3999–4012.

IONESCU-KRUSE, D. 2015 Short-wavelength instabilities of edge waves in stratified water. *Contin. Discr. Dyn. Syst.* **35**, 2053–2066.

KARIMI, H. H. & AKYLAS, T. R. 2014 Parametric subharmonic instability of internal waves: locally confined beams versus monochromatic wavetrains. *J. Fluid Mech.* **757**, 381–402.

KATAOKA, T. & AKYLAS, T. R. 2013 Stability of internal gravity wave beams to three-dimensional modulations. *J. Fluid Mech.* **736**, 67–90.

KLOSTERMEYER, J. 1982 On parametric instabilities of finite-amplitude internal gravity waves. *J. Fluid Mech.* **119**, 367–377.

KLOSTERMEYER, J. 1991 Two- and three-dimensional parametric instabilities in finite-amplitude internal gravity waves. *Geophys. Astrophys. Fluid Dyn.* **61**, 1–25.

KOUDELLA, C. R. & STAQUET, C. 2006 Instability mechanisms of a two-dimensional progressive internal gravity wave. *J. Fluid Mech.* **548**, 165–196.

KUNDU, P. K., COHEN, I. M. & DOWLING, D. R. 2012 *Fluid Mechanics*. Elsevier.

LANDMAN, M. J. & SAFFMAN, P. G. 1987 The three-dimensional instability of strained vortices in a viscous fluid. *Phys. Fluids* **30**, 2339–2342.

LE REUN, T., FAVIER, B. & LE BARS, M. 2018 Parametric instability and wave turbulence driven by tidal excitation of internal waves. *J. Fluid Mech.* **840**, 498–529.

LEBLANC, S. 1997 Stability of stagnation points in rotating flows. *Phys. Fluids* **9**, 3566–3569.

LEBLANC, S. 2004 Local stability of Gerstner's waves. *J. Fluid Mech.* **506**, 245–254.

LIFSCHITZ, A. & HAMEIRI, E. 1991 Local stability conditions in fluid dynamics. *Phys. Fluids* A **3**, 2644–2651.

LOMBARD, P. N. & RILEY, J. J. 1996 Instability and breakdown of internal gravity waves. I. Linear stability analysis. *Phys. Fluids* **8**, 3271–3287.

MACKINNON, J. A. & WINTERS, K. B. 2005 Subtropical catastrophe: significant loss of low-mode tidal energy at $28.9°$. *Geophys. Res. Lett.* **32** (15), L15605.

MATHUR, M., CARTER, G. S. & PEACOCK, T. 2016 Internal tide generation using green function analysis: to WKB or not to WKB? *J. Phys. Oceanogr.* **46**, 2157–2168.

MATHUR, M., ORTIZ, S., DUBOS, T. & CHOMAZ, J. M. 2014 Effects of an axial flow on the centrifugal, elliptic and hyperbolic instabilities in Stuart vortices. *J. Fluid Mech.* **758**, 565–585.

MCCOMAS, C. H. & BRETHERTON, F. P. 1977 Resonant interaction of oceanic internal waves. *J. Geophys. Res.* **82**, 1397–1412.

MCEWAN, A. D. & ROBINSON, R. M. 1975 Parametric instability of internal gravity waves. *J. Fluid Mech.* **67**, 667–687.

MERCIER, M. J., MATHUR, M., GOSTIAUX, L., GERKEMA, T., MAGALHÃES, J. M., DA SILVA, J. C. B. & DAUXOIS, T. 2012 Soliton generation by internal tidal beams impinging on a pycnocline: laboratory experiments. *J. Fluid Mech.* **704**, 37–60.

MIED, R. P. 1976 The occurrence of parametric instabilities in finite-amplitude internal gravity waves. *J. Fluid Mech.* **78**, 763–784.

MIYAZAKI, T. 1993 Elliptical instability in a stably stratified rotating fluid. *Phys. Fluids* A **5**, 2702–2709.

MIYAZAKI, T. & FUKUMOTO, Y. 1992 Three-dimensional instability of strained vortices in a stably stratified fluid. *Phys. Fluids* A **4**, 2515–2522.

NAGARATHINAM, D., SAMEEN, A. & MATHUR, M. 2015 Centrifugal instability in non-axisymmetric vortices. *J. Fluid Mech.* **769**, 26–45.

NAYFEH, A. H. & MOOK, D. T. 1995 *Nonlinear Oscillations*. Wiley.

PHILLIPS, O. M. 1977 *The Dynamics of the Upper Ocean*. Cambridge University Press.

RUDNICK, D. L., BOYD, T. J., BRAINARD, R. E., CARTER, G. S., EGBERT, G. D., GREGG, M. C., HOLLOWAY, P. E., KLYMAK, J. M., KUNZE, E., LEE, C. M., LEVINE, M. D., LUTHER, D. S., MARTIN, J. P., MERRIFIELD, M. A., MOUM, J. N., NASH, J. D., PINKEL, R., RAINVILLE, L. & SANFORD, T. B. 2003 From tides to mixing along the Hawaiian ridge. *Science* **301** (5631), 355–357.

SIPP, D. & JACQUIN, L. 2000 Three-dimensional centrifugal-type instabilities of two-dimensional flows in rotating systems. *Phys. Fluids* **12**, 1740–1748.

SONMOR, L. J. & KLAASSEN, G. P. 1996 Higher-order resonant instabilities of internal gravity waves. *J. Fluid Mech.* **324**, 1–23.

SONMOR, L. J. & KLAASSEN, G. P. 1997 Toward a unified theory of gravity wave stability. *J. Atmos. Sci.* **54**, 2655–2680.

STAQUET, C. & SOMMERIA, J. 2002 Internal gravity waves: from instabilities to turbulence. *Annu. Rev. Fluid Mech.* **34**, 559–593.

TABAEI, A. & AKYLAS, T. R. 2003 Nonlinear internal gravity wave beams. *J. Fluid Mech.* **482**, 141–161.

THORPE, S. A. 1994 Statically unstable layers produced by overturning internal gravity waves. *J. Fluid Mech.* **260**, 333–350.

VARMA, D. & MATHUR, M. 2017 Internal wave resonant triads in finite-depth non-uniform stratifications. *J. Fluid Mech.* **824**, 286–311.